FIBER OPTIC SENSORS FOR ON-LINE, REAL TIME POWER TRANSFORMER HEALTH MONITORING

Bo Dong

Dissertation submitted to the Faculty of the
Virginia Polytechnic Institute and State University
in partial fulfillment of the requirements for the degree of

DOCTOR OF PHILOSOPHY

in

Electrical Engineering

Anbo Wang, Chair
Gary S. Brown
James R. Heflin
Gary R. Pickrell
Yong Xu

August 9, 2012
Blacksburg, Virginia

Key words: **Partial discharge, fiber optic sensor, acoustic sensor, dissolved gas analysis.**

FIBER OPTIC SENSORS FOR ON-LINE, REAL TIME POWER TRANSFORMER HEALTH MONITORING

Bo Dong
Electrical Engineering
(ABSTRACT)

High voltage power transformer is one of the most important and expensive components in today's power transmission and distribution systems. Any overlooked critical fault generated inside a power transformer may lead to a transformer catastrophic failure which could not only cause a disruption to the power system but also significant equipment damage. Accurate and prompt information on the health state of a transformer is thus the critical prerequisite for an asset manager to make a vital decision on a transformer with suspicious conditions.

Partial discharge (PD) is not only a precursor of insulation degradation, but also a primary factor to accelerate the deterioration of the insulation system in a transformer. Monitoring of PD activities and the concentration of PD generated combustible gases dissolved in the transformer oil has been proven to be an effective procedure for transformer health state estimation. However current commercially available sensors can only be installed outside of transformers and offer indirect or delayed information.

This research is aimed to investigate and develop several sensor techniques for transformer health monitoring. The first work is an optical fiber extrinsic Fabry-Perot interferometric sensor for PD detection. By filling SF_6 into the sensor air cavity of the extrinsic Fabry-Perot interferometer sensor, the last potential obstacle that prevents this kind of sensors from being installed inside transformers has been removed. The proposed acoustic sensor multiplexing system is stable and more economical than the other sensor multiplexing methods that usually require the use of a tunable laser or filters. Two dissolved gas analysis (DGA) methods for dissolved hydrogen or acetylene measurement are also proposed and demonstrated. The dissolved hydrogen detection is based on hydrogen induced fiber loss and the dissolved acetylene detection is by direct oil transmission measurement.

ACKNOWLEGEMENT

First of all, I would gratefully thank my advisor, Dr. Anbo Wang, for all of his professional guidance, advices, enormous encouragements, heuristic education, and continuous support technically and financially. With his confidence, determination, dedication, and incredible achievements, he will continue to serve as my mentor who sheds light on my journey ahead. He is really a great teacher.

I am also grateful to all the committee members, Dr. Gary Brown, Dr. Randy Heflin, Dr. Ira Jacobs, Dr. Gary Pickrell and Dr. Yong Xu for serving on my committee and for the encouragement and valuable suggestions that I received from them.

Very special thanks go to Dr. Luke van der Zel with EPRI for his continuous supporting on every direction of this research. His management and suggestions on all of these projects are efficient and invaluable.

In addition, thank very member in CPT group, such as Ming Han, Jianmin Gong, Chennan Hu, Tyler Schillig, Alan Overby, Yizheng Zhu, Juncheng Xu, Cheng Ma, Evan Lally, Yongxin Wang, Jiajun Wang, Yunjing Wang, Yumiao Wang, and so on. They are all my sincere friends, their help on my research and life is unforgettable and discussions with them are very beneficial.

Finally, I would like to give special thanks to my parents, grandparents, uncles, aunties and brother who have always been there when I needed with constant support and guidance. Love you guys.

All photos by author, 2012.

TABLE OF CONTENTS

List of Figures

LIST OF TABLES

CHAPTER 1

Introduction

High voltage transformer is one of the most important and expensive devices in the power industry. In high voltage transformers, a decisive significance is attributed to a secure and permanent insulation. However, under operating conditions the electrical, thermal and mechanical aging affects the insulating medium inside a high voltage transformer. Partial discharge (PD) is not only a precursor of insulation degradation, but also a primary factor to accelerate the deterioration of the insulation system in a transformer. If this incipient omen were missed or ignored, the direct incoming consequence could be a possible succeeding insulation breakdown and catastrophic failures, and the cost of each failure can easily drive the total cost of a single transformer failure into multi-million dollars. Therefore, to accurately monitor the health state of transformers and predict incipient fatal failures has always been a primary goal for the transformer industry to pursue.

1.1 Background of Transformer Health State Monitoring

Although in a high voltage power transformer the insulation system, which includes both the structures and materials, is carefully designed with sufficient margins, the numerous inevitable mechanical, thermal, and electrical stresses that these transformers undergo during their entire life of service often give rise to a degradation of the insulation system. Thermal faults (hot-spots) and electrical faults (PDs) are the two major mechanisms that can lead to premature insulation breakdown and catastrophic transformer failures. The consequence of an unexpected transformer failure or outage can be dire in both safety and

financial terms. From 1997 to 2001, the average age of the transformers that failed by insulation failures was 18 years and its average cost was more than six million dollars[1]. Therefore research is important on the detection of hot-spots and PD activities to identify incipient insulation problems so that remedial action can be taken to prevent catastrophic failures.

The insulations inside a high power transformer, such as the transformer insulation liquid, the bonding epoxy, and the coating of the windings, experience tremendous electrical stress, and sometimes thermal stresses. Due to the aging effect, the electrical strength of these insulations gradually deteriorates. When the dielectric strength decreases to a certain level, partial discharge occurs; therefore, by detecting the activities of partial charges in a transformer, the risk of an imminent transformer failure can be evaluated. Not only do partial discharge activities provide early warning of imminent transformer failures, but they also accelerate the breakdown process. For example, the repeated arcing between the ground and the conductor will reduce the mechanical strength of the bonding between the coating and the winding and also reduce the dielectric strength of the insulation.

A variety of physical-chemical diagnostic methods have been developed and introduced into regular use to determine the health condition of power transformers. One of these methods is dissolved gas analysis (DGA) that makes use of the fact that gas is generated when an electrical arc or overheating develops inside the transformer. In this method sampling of transformer oil as well as the gas analysis can be carried out during the operation of the transformer. Although laboratory DGA has been the traditional practice, there is a drawback related to this method: the method is time consuming. The process involves sampling, shipping, and analyzing in lab; it may take several days to complete the test and obtain the result. Moreover, the cost for a test is high because of the complicated procedure and the involvement of much labor resource. The prevailing of portable DGA instruments, to some extents, shortens the timeframe between samples, but some critical rapid developing faults, which deteriorate in a few days or weeks, still can be missed by the relatively long sample periods.

Another category of methods for transformer health assessment is to monitor the partial discharges on line with different built-in sensors directly in the transformers. When a

partial discharge occurs inside a transformer, the electricity emitted from the conductor disturbs the molecules of the transformer liquid and therefore generates ultrasonic waves, which are transmitted throughout the transformer via the oil medium. The ultrasonic waves provide an effective means for on-line partial discharge monitoring. Presently commercial available detectors for this purpose are piezoelectric acoustic sensors. Because of the strong electromagnetic interference (EMI) inside transformer tanks and short circuit potential, these sensors have most commonly been mounted on the outside wall of the transformers which makes them suffered from 20dB acoustic wave energy loss due to the reflection on the oil and steel interface[2].

1.2 Advantages of Fiber Optic Sensors

Fiber-optic sensors are an excellent candidate for on-line monitoring of both the acoustic waves and the dissolved gasses inside a power transformer. Fiber-optic sensors made from dielectric materials, such as fused-silica glass, are inherently immune to the EMI. Many fiber-optic sensors have been developed for measurement of acoustic waves and gases. Besides the advantages of small size, light weight, and high sensitivity, these sensors have a potential to be placed inside the transformer tank without affecting the performance of the sensors and the insulation integrity of the transformers. This is of great importance as for both the gas and acoustic wave detections. The gases can be monitored on-line and in real time. The result can be intermediately and continuously obtained and the cost is much reduced by eliminating the sampling, shipping, and lab work in the traditional DGA process. The partial discharge detection is more sensitive as much stronger ultrasonic waves are present inside the transformer. Moreover, fiber-optic sensors have the great potential of multiplexing which means that distributed electrical and thermal fault detection could be achieved with a single signal conditioner, providing the temperature profile of the winding and enabling the localization of the partial discharge origin. Furthermore, the multiplexing capability may significantly reduce the system design complexity and cost.

1.3 Outline of the Dissertation

The ultimate goal of this Ph.D. dissertation is to design, fabricate and test fiber optic sensors that can be installed inside power transformers to realize on-line and real time monitoring of partial discharge events by acoustic signal and dissolved gases detection at the first locale. The corresponding data acquisition systems and signal processing methods are also researched to increase detection sensitivity and reliability and, meanwhile, decrease the system cost.

On-line and inside-transformer acoustic partial discharge detection and dissolved gases analysis are the two mainly aspects of this research. In Chapter 2, the design of a diaphragm based extrinsic Fabry-Perot interferometer (EFPI) PD sensor that can resist high electric stress inside power transformers is presented. Chapter 3 gives the design of a low cost multiplexed EFPI PD sensor interrogation system. Chapter 4 presents the a fiber optic sensor for dissolved hydrogen detection and some preliminary results. In Chapter 5 a sensor for the detection of acetylene dissolved in transformer oil and related preliminary results are given. Finally, Chapter 6 presents the summary of this research.

CHAPTER 2

EFPI Acoustic Partial Discharge Sensor

The diaphragm based EFPI acoustic sensor has obvious advantages over other sensors for detection of PD events in power transformers. Current EFPI sensor designs have an inevitable air-filled cavity. Owing to its small dielectric strength, the air trapped in the Fabry-Perot (FP) cavity could potentially result in partial discharges inside the sensor and becomes a major barrier to the field application of this kind of sensors inside high voltage power transformers. To overcome this problem, an EFPI sensor with its cavity filled with sulfur hexafluoride (SF_6) is designed, fabricated and tested.

2.1 Comparison of Current PD Detection Methods

A partial discharge is a localized dielectric breakdown which occurs at a small portion of the electrical insulation system and it does not bridge the electrodes. Because the dielectric insulation, which can be composed of solid, liquid or gaseous insulators, usually is not homogeneous, some local weak points ionized earlier at relatively low electric stress that other portions can still resist. The newly formed electrons gain energy in the applied electric field and ionize more molecules by impact, therefore an avalanche is formed[3]. Because of the movement of these electrons and ions towards opposite electrodes, a transient current can be detected in the circuit loop which connects the two electrodes. Although the magnitude of PDs is usually small, they cause progressive deterioration on the insulation system which can lead to the ultimate failure of the transformer[3, 4].

Usually PDs in a transformer insulation system only occur under high electric stress

therefore the energy release during the discharge is sufficiently high to give rise to many detectable physical and chemical phenomena, such as electric pulses, radio frequency emission, acoustic emission, light, heat and chemical transformations [5, 6]. In a retrospect of more than four decades of PD detection history, an abundance of methods have been developed, but they can be simply grouped into four categories as electrical, optical, acoustic and chemical detection [7, 8].

A. Electrical Method

The electrical detection measures the apparent charge induced current impulse in a PD event and it can be subdivided into electric current impulse detection and ultra-high frequency (UHF) radiation detection. For the current impulse method known as conventional method, as suggested in standard IEC 60270 [9], a coupling capacitance (or quadrupole) is connected the to the unit under test (UUT) to detect the PD current passing through the network of coil and the earth line. The UHF detection relies on UHF antennas to capture PD induced resonance up to 1.5GHz with PD source locating capability [10, 11]. This method is widely used by transformer manufacturers since it is sensitive but it is not suitable for operating transformer monitoring because of its susceptibility to noise.

B. Optical Method

The optical detection represents the methods that detect the optical radiation during PD events. For the enclosed and light tight transformer application, either a lens system or a special fluorescent fiber is used to couple the emitted light into the core of conventional optical fibers, and then the spectral and timing information of the collected light are analyzed to get properties of the discharge [12, 13]. Usually the sensor cannot be installed to have a clear view of PD sources and most of the insulation materials are lossy in the detection spectrum range so its application is quite limited [14].

C. Acoustic Method

The heat released during a PD activity can evaporate local insulating material and generate a small explosion which emits detectable ultrasonic waves that propagate throughout the insulation. Although the acoustic detection method cannot measure the apparent charge quantitatively [8], its attractive advantages, such as insensitivity to EMI,

PD source locating capability and instantaneous response to PD activities, have made it the first choice for on-line, real time transformer health monitoring. Traditionally, piezoelectric sensors are used for this purpose [6, 15], but these sensors can only be installed outside of the transformer which degrades their sensitivity and locating capability, therefore, in recent years, fiber optic acoustic sensors have been pulling more interests of researchers. Early fiber optic acoustic sensors for PD detection in transformers were based on all-fiber intrinsic Michelson or Mach-Zehnder interferometric (MZI) technology [3, 16, 17]. Because the fiber length in the sensing arm, the fiber coil, needs to be adequate long, say 10 to 100 meters, to meet the sensitivity requirement which is about 1 Pa, these sensors usually suffer from fringe fading problems due to random polarization rotation and severe quadrature point (Q-point) drifting problems caused by temperature induced optical path length (OPD) changes. To overcome these problems, people use fiber optic EFPI sensors which are implemented on a very small sensing element known as the Fabry-Perot (FP) cavity which is formed by two reflecting surfaces [7, 18-20]. Since the typical FP cavity length, or the sensing arm, is less than 100 microns, which is less than 10^{-5} of that in the previous structures, sensor stability has been tremendously improved. Moreover an EFPI acoustic sensor only has 10^{-2} of the size of a fiber coil sensor head, which is an obvious advantage for inside transformer installation.

D. Chemical Method

One of the consequences of PDs is chemical change of material. Dissolved gas analysis (DAG), which analyzes the concentrations of PD generated combustible gases and their ratios, is still always the single best indicator of a transformer's overall condition since its debut in the 1960s and many IEEE and ICE guides are formed for this purpose [21-24]. Chemical testing has some limitations that prevent it from being the only method used for PD detection. The first, it does not instantly response to the PD activities. Lab DAG or current on-line DAG equipments take oil samples from the maintaining port of the transformer, so the PD generated gases need to accumulate to the detectable level and circulate with oil to the maintenance port to be detected. The second, chemical testing does not provide any information about the position of the PD. Therefore it is better for the

transformer asset manager to collect both the DAG and PD events information to diagnose faults occurred in transformers and prevent the catastrophic failures.

Based on the comparison above, it can be easily seen that the fiber optic EFPI acoustic sensor is the most promising sensor that can be installed inside transformers to realize on-line and real time PD activities monitoring.

2.2 Theoretical Analysis of Sensor Breakdown Stress

As shown in Figure 2-1, current EFPI acoustic sensors have an inevitable air-filled cavity. Owing to its small dielectric strength, the air trapped into the FP cavity of an EFPI sensor could potentially result in partial discharges inside the sensor and become a major concern on installing this kind of sensors inside high voltage power transformers. Sulfur hexafluoride (SF_6), the most commonly used insulation gas in industry, has a dielectric strength 2.5 times as that of dry air. In addition to its high electric strength, SF_6 has excellent arc-quenching properties and is colorless, nontoxic, and non-inflammable, and it has no absorption line around the working optical wavelength of 1550nm. All of these make it a good choice to fill in the FP cavity to increase the dielectric strength of the sensor head.

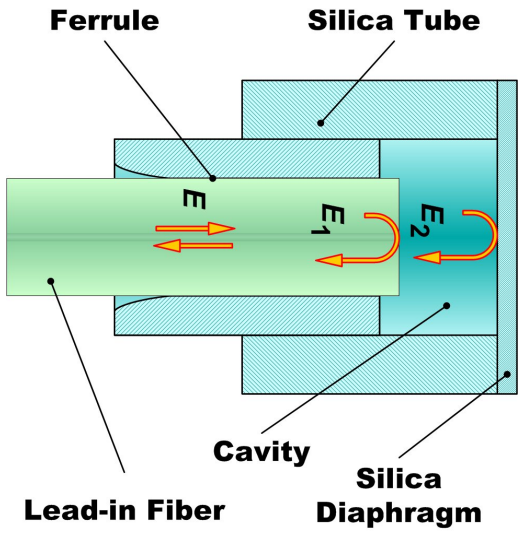

Figure 2-1: Traditional EFPI acoustic FP sensor structure.

Because the FP cavity is in the shape of a very thin circular disk, when the applied electric field is perpendicular to the axis of the disk, the field inside the void is approximately the same as that in the transformer oil [25]. But when its axis is parallel to the field, the ratio between the electric stress in the void and that in the transformer oil is inversely propositional to the ratio of their permittivities. Given that the relative permittivity of transformer oil is around 2 and typically, the electric filed intensity, E, in an operating power transformer is less than 6kV/mm [26], the void should be able to resist stress of at least 12 kV/mm. If a factor of safety of 3 is applied, the designed stress for the FP cavity is not less than 36kV/mm at power frequency.

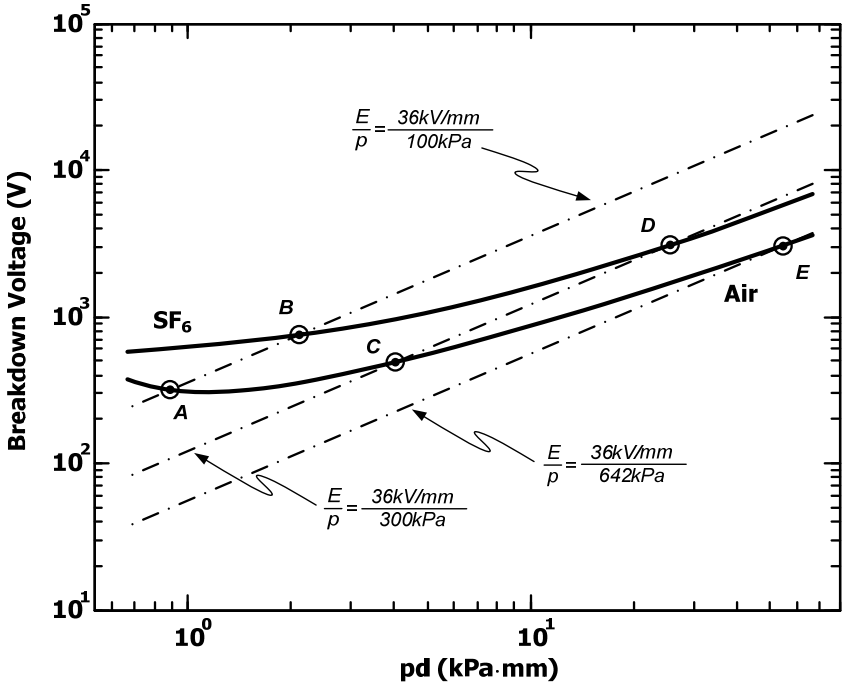

Figure 2-2: Breakdown voltage versus *pd* characteristics (Paschen curves) for SF_6 and dry air.

Paschen's law indicates that the breakdown potential varies as the product of gas pressure, p, and electrode separation, d in uniform field gaps. Figure 2-2 shows the Paschen curves of SF_6 [27] and dry air [28] at 20°C with lines of E/p at three different levels. The parameters of interested crossing points are given in the graph. Within the range of Figure 2-2, it is obvious that if the pressure of the gas keeps constant, the breakdown electric filed intensity increases as the gap distance decreases.

Table 2-1: Parameters of crossing points under interest.

Points	U (V)	E (kV/mm)	pd (kPa·mm)	p (kPa)	d (mm)
A	315	36	0.88	100	0.009
B	762	36	2.2	100	0.02
C	483	36	4.0	300	0.01
D	3060	36	25	300	0.09
E	3060	36	55	642	0.09

At atmospheric pressure, the maximum required gap distances to resist stress of 36kV/mm for air and SF_6 are 0.009mm and 0.02mm respectively, which are very difficult to control in the sensor fabrication because during the laser bonding process, the diaphragm can easily deform and contact the ferrule top which makes no room for the diaphragm to respond to the pressure variation applied on it. To our best estimation, gap distance around 0.1mm is feasible, which corresponds to points D and E in Table 2-1. Obviously, the pressure of SF_6 at point D, which is around 3atm, is of more operability than that of the air at point E, which is more than 6atm. Because the breakdown stress of SF_6 between dielectric coated electrodes, which is similar to the condition of fused silica sealed void, is 30~88% higher than that with bare electrodes [29], the theoretical breakdown stress for the optical PD sensor with a 0.1mm FP cavity filled with SF_6 at 300kPa is more than 47kV/mm.

2.3 Improved Sensor Structure Design

Since sensor heads composed from parts with different materials usually suffer thermal stress and temperature instability, as shown in Figure 2-3, the new sensor head is designed to be made with only fused silica parts, including a piece of wafer, a sleeve and a ferrule. Furthermore CO_2 laser thermal welding technique[30] is used to minimize the sensor cavity drifting caused by bonding adhesives, such as epoxies or borosilicate powders[19]. Because it is rather difficult to bond these parts in a 300kPa SF_6 environment, we propose to use a piece of special fiber, a side-hole single mode fiber (SMF) as the lead in fiber to the sensor head. After sensor fabrication, the sensor head cavity is vacuumed and filled with SF_6 through the two channels of the side-holes of the fiber and finally the side-hole

channels are sealed by splicing a segment of a regular singlemode fiber (SMF).

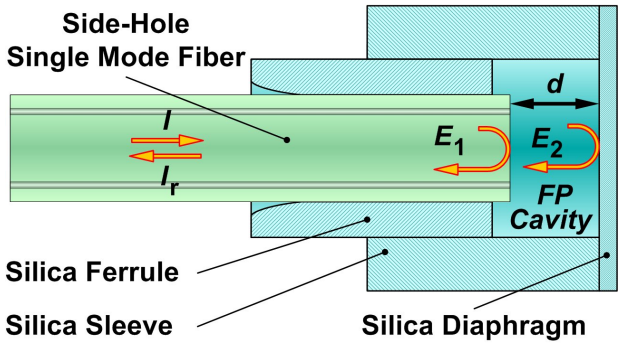

Figure 2-3: Schematic of the improved sensor head structure.

2.4 Sensor Fabrication

Figure 2-4(a) and (b) illustrate the sensor head structure before and after the laser thermal welding respectively and Figure 2-4(c) is the picture of a real sensor head. Dimensions of key components of the sensor head are listed in Table 2-2.

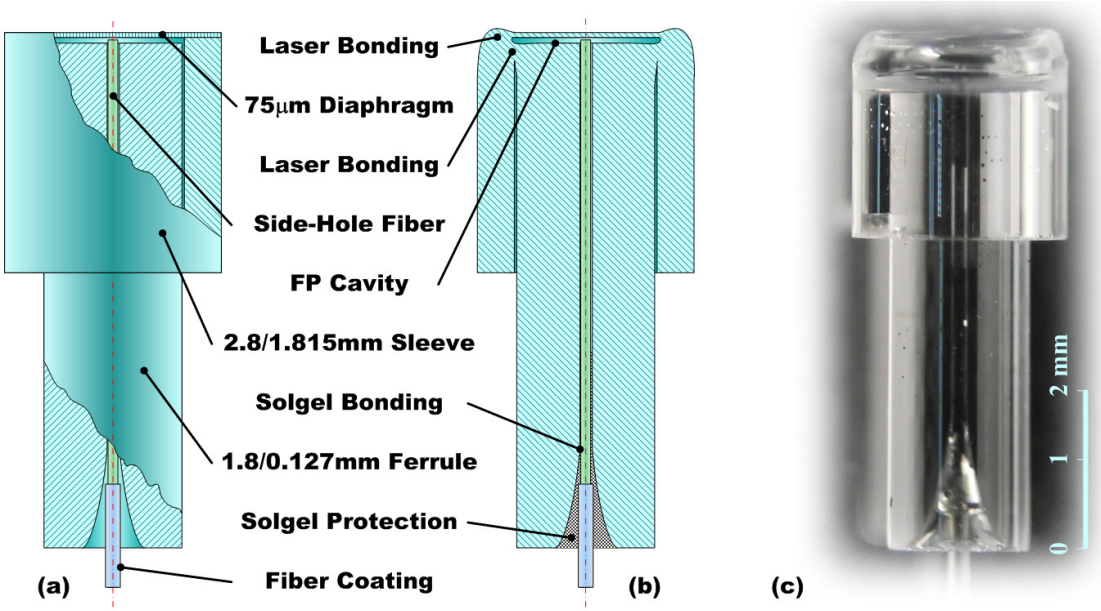

Figure 2-4: Sensor head structure and bonding; (a) sensor head structure; (b) cross-section view of the sensor head after laser and sol-gel bonding; (c) a real sensor picture.

Table 2-2: Dimensions of key components of the sensor head

Item	I.D. (μm)	O.D. (mm)	Length (mm)
Ferrule	127	1.8	6
Sleeve	1815	2.8	3

A fused silica pressure sensor bonding setup made by previous researchers at the Center for Photonics Technology (CPT) of Virginia Tech was modified for the new sensor fabrication purpose, which is shown in Figure 2-5(a). To make a PD sensor, firstly, a ferrule and a sleeve were mounted on the top of a rotation stage rotating at 120rpm and then a 7W 10μm CO_2 laser beam was focused down to a ϕ0.2mm spot to heat the contacting corner of the ferrule and sleeve with 30° incident angle. It took about 40 seconds to thermally weld these two parts together, which included two ten-second linear ramping stages for power rising and falling respectively. The rotation stage was then adjusted to its vertical position and a piece of 75μm fused silica wafer cut into 2×2mm square was put on top and welded to the ferrule and sleeve assembly. The entire welding process was watched with a long working distance microscope and a monitor. At last a piece of side-hole fiber (Figure 2-5 (b) shows its cross-section view) with removed jacket and cleaved end was inserted into the bonded sensor head. The cavity length between the fiber tip and the inner surface of the diaphragm was adjusted to the desirable value using a translation stage. Then glass sol-gel was placed at the flare of the ferrule and a low power CO_2 laser was applied to solidify the sol-gel. Because the bonding temperature was low, the fiber and its coating were still intact after bonding.

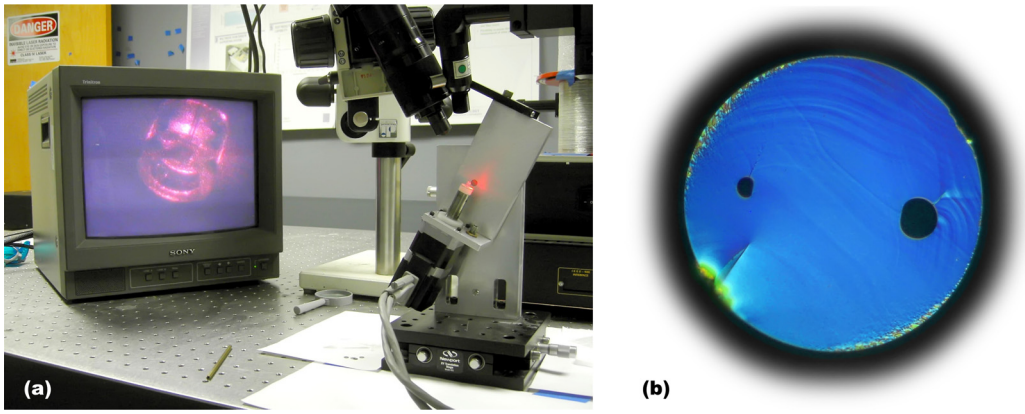

Figure 2-5: (a) Sensor CO_2 bonding system; (b) cross-section view of the side-hole SMF.

The side-hole fiber used here is the same as a single mode fiber except that in the cladding area, there are two air channels along the axis of the fiber, through which SF_6 can be filled into the FP cavity after the sensor fabrication. The schematic of SF_6 inflation system is shown in Figure 2-6. First valve V2 was turned off and valve V1 was turned on. The air trapped in the sensor head during the first part of the fabrication was sucked out by a vacuum pump. Then value V1 was turned off and valve V2 was turned on to let the compressed SF_6 enter the sensor head through the air channels of the side-hole fiber. This procedure can be repeated several times to ensure the high pure concentration of SF_6 in the sensor head. Because the diameters of the air channels are only 8 or 16 μm, it took around 30 min for the pressure inside the sensor head and in the gas chamber to become balanced. After fabrication, the side-holes of the sensor were sealed by splicing the fiber with a span of regular fiber.

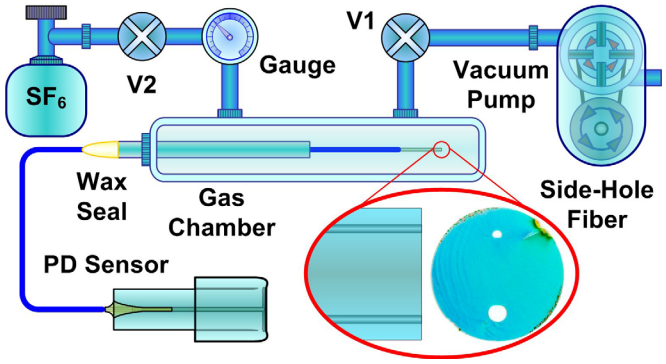

Figure 2-6: Schematic of SF_6 inflation system.

2.5 PD Threshold Test System

Based on ASTM D877-02, a standard to test the dielectric breakdown voltage of insulating liquids, we designed a simplified setup as shown in Figure 2-7 and Figure 2-8. The two electrodes were made from two parallel alumina disks of 35mm in diameter separated by a distance of 3mm. The sensor was partially embedded into the ground electrodes. The distance between the sensor end and the other electrode was about 0.6 mm. The electrodes were connected to a 60 Hz AC high voltage supply, PFT-303CM (High Voltage Inc.), with output voltage continuously adjustable from 0 to 30kV (rms value). The dielectric strength of the insulating fluid used in the test, Galden D02, is 40kV (2.54mm gap). Two

PZT transducers (Model: WDU, Physical Acoustic Co.) were used, with one mounted at the side wall of the test container as a PD acoustic signal simulator and the other mounted at the center bottom of the test tank as a PD sensor. The gain of the following bandpass amplifier (PAC 1220A) was set at 60dB. Lubricating grease was used between the transducers and the test tank to enhance the acoustic coupling efficiency. A capacitor (0.1μF) was placed beneath the test container to monitor the sparks, arcing, or other electromagnetic fluctuations. The amplified PZT PD sensor signal and the electromagnetic sensor signal were sent to a two-channel oscilloscope triggered at normal mode to monitor the occurrence of the PD.

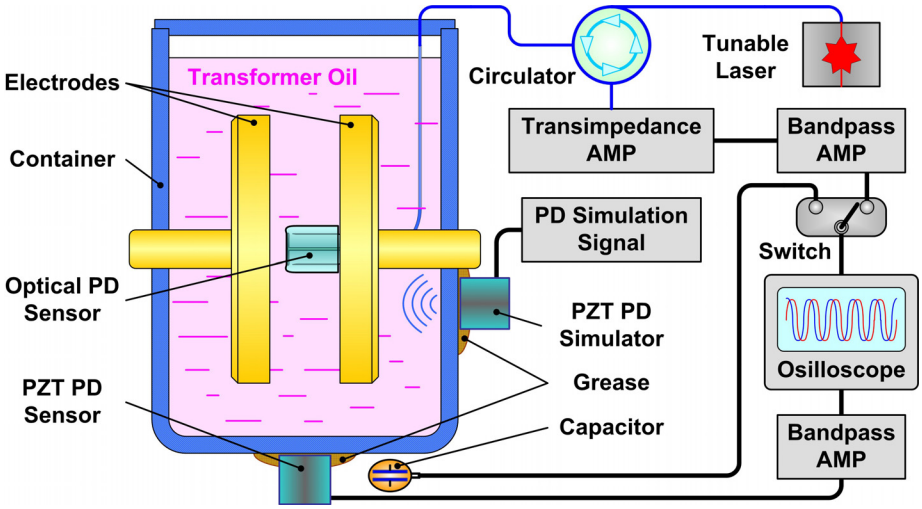

Figure 2-7: Schematic of PD sensor breakdown voltage test system.

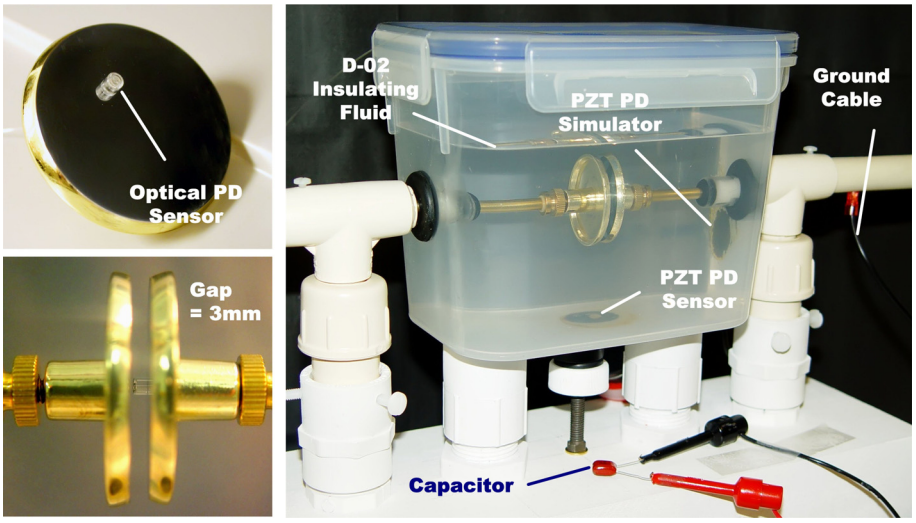

Figure 2-8: Pictures of the PD threshold test container.

2.6 Test Procedure and Results

The test procedures are as follows: First, we tested the insulating fluid at the highest available voltage (30kV) before the optical sensor was mounted onto the electrode. Second, we mounted an optical sensor with its FP cavity filled with air at atmospheric pressure and measured its PD threshold voltage. Third, we filled the FP cavity with SF_6 at two different pressures (200 and 300 kPa) and measured its PD threshold voltage at each pressure. During the test, the voltage applied on the electrodes was increased gradually at a step of 2kV. At each step the voltage was maintained constant for at least 2 minutes to check for PD activities before increasing the voltage to the next level. If a PD was observed, the current voltage was recorded as the PD threshold voltage of the sensor under test.

When the voltage was higher than 20 kV, we observed very strong corona at the cable connections between the test setup and the high voltage power supply that were exposed to air. These sparks were not only captured by the detecting capacitor placed out of the test tank but also coupled into the acoustic PZT sensor. Fortunately, the corona can be discriminated from a true PD signal by the spike-like feature of the corona signal, as shown in Figure 2-9(a) and (b). When the optical sensor was filled with 100-kPa air, PD occurred at 10 kV (shown in Figure 2-9(b)). Figure 2-9(c) and (d) are for the sensor filled with 200-kPa SF; it is shown that PDs occurred at 24 kV. The test results for the sensor filled with 300-kPa SF is shown in Figure 2-9(e); no PD occurred up to 30 kV (the output limit of the power supply), indicating that the SF -filled sensor was at least three times larger than the traditional air-filled sensor. Finally, we used the PZT transducer to generate a simulated PD signal at high voltage; both the PZT sensor and the optical sensor filled with 300-kPa SF successfully detected the signal as shown in Figure 2-9(f), which proved that the test was valid and the SF –filled sensor functioned normally at high voltage environment[31].

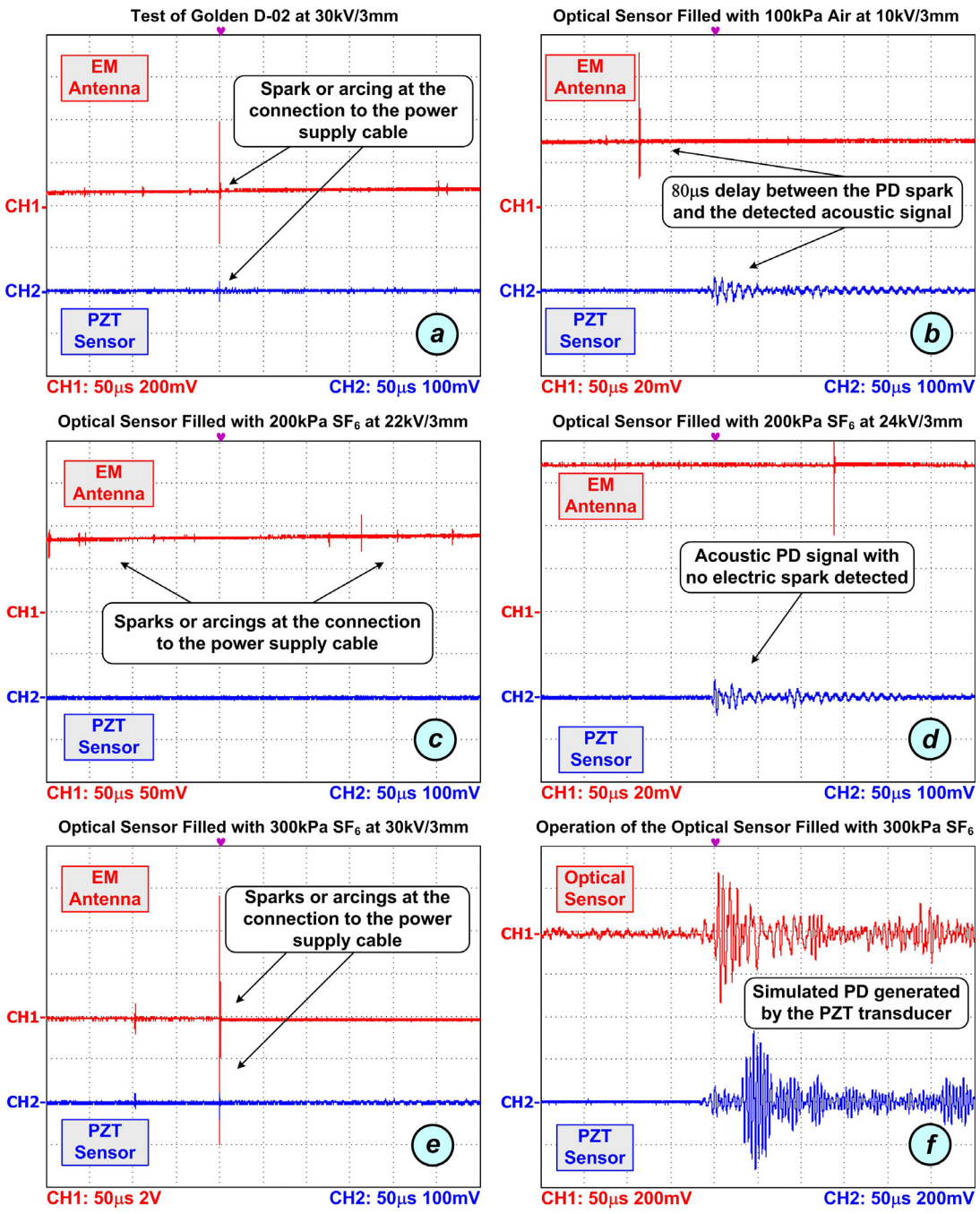

Figure 2-9: Test results of D-02 insulating fluid and optical sensor with different fillings.

CHAPTER 3

Low Cost EFPI Acoustic PD Sensor Multiplexing System

When an EFPI acoustic sensor discussed in Chapter 2 is installed in a power transformer, due to the thermal expansion and the static background pressure of the transformer oil, the original cavity length or the working point may drift from the optimized quadrature point (Q-point), which causes degradation in the sensor sensitivity. Previously a tunable laser or filter is used to adjust the wavelength of the probing light according to the sensor cavity length[19], which dictates the system high cost. Also this approach makes sensor multiplexing difficult because in such a multiple-sensor system, each sensor needs a dedicated tunable laser or a tunable filter otherwise the 50μs duration of a PD event can be easily missed. Quadrature detection has been proven to be an efficient method to solve the Q-point drifting induced signal fading in interferometers[32]. Two quadrature phase-shifted signals can be acquired by modifying the interferometer structure, such as introducing an additional interfering channel[33-36] or using special coupler structures[37-42], which obviously increases the sensor fabrication complexity. However, another approach, which probes the interferometer with light at two different wavelengths followed with the arctan algorithm to recover the real signal[43-49], is adopted for the construction of a low-cost multipled sensor system. Based on this method, a 4-channel FP acoustic sensor system for multiple point PD detection in power transformers is proposed.

3.1 Sensing Principle of the Sensor

As shown in Figure 3-1, the FP cavity is formed by a cleaved end of a single mode fiber and the inner surface of a thin fused-silica diaphragm. The silica sleeve and the silica

ferrule facilitate the alignment of the fiber and the support of the diaphragm. The incipient light from the fiber is partially reflected by the two surfaces of the cavity due to the Fressnel reflections at the glass-air interfaces. The two reflections then interfere with each other and the interference signal contains the information of the FP cavity length. When PD activities occur, the PD-generated acoustic waves cause the diaphragm, and consequently the FP cavity length, to vibrate. By measuring the cavity length variations from the interference signal, the acoustic waves, and consequently the PD, can be detected.

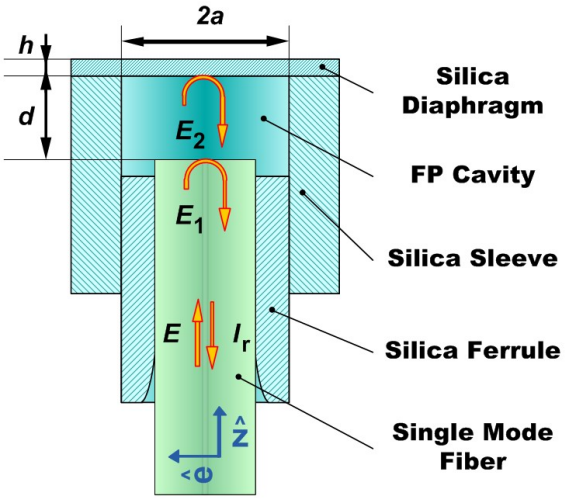

Figure 3-1: Typical structure of a diaphragm based EFPI acoustic sensor

Assume the electrical field of the incipient light is **E**, and the electrical field of the reflections from the fiber end and inner surface of the diaphragm are $\mathbf{E}_1$ and $\mathbf{E}_2$, respectively. Electrical field $\mathbf{E}_1$ can be expressed as

$$\mathbf{E_1} = E_1\hat{\mathbf{e}} = A_1 e^{j(\omega t - \beta z + \phi)}\hat{\mathbf{e}} \tag{3.1}$$

where β is the propagation constant of the light in the fiber, A_1, ω, and ϕ are the amplitude, the angle frequency, and the initial phase of the light, respectively. Since the electric field $\mathbf{E}_2$ travels an extra distance ($2d$) inside the cavity and then couples back to the SMF, compared to $\mathbf{E}_1$, it has a relative phase shift of $4\pi d/\lambda_0$, where λ_0 is the wavelength of the light in air and d is the FP cavity length. Therefore, $\mathbf{E}_2$ can be written as

$$\mathbf{E}_2 = E_2\hat{\mathbf{e}} = A_2 e^{j(\omega t - \beta z + \phi - 4\pi d/\lambda_0 + \pi)}\hat{\mathbf{e}} \tag{3.2}$$

where A_2 is the amplitude of the light and the extra phase shift of π arises from the

reflection at the diaphragm surface of light incident from a medium that is optically less dense to a medium that is optically denser. Since the reflections at both FP surfaces are small (~4% governed by the Fressnel law), the multi-reflections inside the FP cavity can be ignored. The interference signal is detected by a photodetector and the output of the detector is then approximately given by

$$\begin{aligned} I_r &\approx \left|\mathbf{E_1} + \mathbf{E_2}\right|^2 = \left(E_1 + E_2\right)\left(E_1 + E_2\right)^* \\ &= A_1^2 + A_2^2 - 2A_1A_2\cos(4\pi d / \lambda_0) \end{aligned} \tag{3.3}$$

After filtering out the direct current (DC) signal, the useful alternative current (AC) is given by

$$U\left(t\right) = \gamma\cos\left[4\pi\left(d_0 + \delta\left(t\right)\right)/\lambda_0\right] \tag{3.4}$$

which is a function of both cavity length $d = d_0 + \delta(t)$ and light wavelength λ_0, and γ is a constant. Since FP cavity length variation $\delta(t)$ caused by the PD-generated acoustic wave is much smaller than both the initial cavity length d_0 and the probing light wavelength λ_0, the sensitivity of the sensor, which is defined as the intensity change caused by unit cavity length change, is given by

$$S\left(d\right) = \frac{\partial U}{\partial d} = \gamma'\sin\left(4\pi d_0 / \lambda_0\right) \tag{3.5}$$

where $\gamma' = 4\pi\gamma / \lambda_0$. Eq.(3.5) shows that the sensor sensitivity corresponding to the gap-length is sinusoidal function of the gap length and reaches its maximum when

$$d_0 = d_{Qm} = \left(m + \frac{1}{2}\right)\frac{\lambda_0}{4} \quad m = 0, 1, 2... \tag{3.6}$$

These d_{Qm} are called quadrature operating points or Q-points of the sensor and the sensor response is approximately linear in the vicinity of each d_{Qm}.

3.2 Two-wavelength Quadrature Demodulation

Two-wavelength quadrature demodulation uses two lasers with different wavelengths as the interrogating light. Assume an arbitrary wavelength $\lambda=\lambda_0+\delta\lambda$, where $\delta\lambda$ is the deviation from a reference wavelength λ_0 and satisfies $\delta\lambda << \lambda_0$; then from Eq.(3.4), the normalized response of the sensor is approximately a cosine function of $\delta\lambda$ which is given by

$$\begin{aligned} U(\lambda_0+\delta\lambda, d) &\doteq \cos\left[4\pi d\left(\frac{1}{\lambda_0}-\frac{\delta\lambda}{\lambda_0^2}\right)\right] \\ &= \cos\left(\theta - 4\pi d\cdot\delta\lambda/\lambda_0^2\right), \end{aligned} \tag{3.7}$$

where $\theta=4\pi d/\lambda_0$. The period of the cosine function in Eq.(3.7) is

$$\Lambda_d = \frac{\lambda_0^2}{2d} \tag{3.8}$$

Figure 3-2(a) and (b) shows the normalized sensor response as a function of the laser wavelength change at two different cavity lengths d and d'. When $|d-d'| << d$, the periods of the sinusoidal curves shown in Figure 3-2(a) and (b) are approximately equal. In two-wavelength quadrature demodulation, the wavelengths of the lasers, λ_1 and λ_2 are selected in such a way that

$$\delta\lambda = \lambda_2 - \lambda_1 = \frac{\Lambda_d}{4} = \frac{\lambda_0^2}{8d} \tag{3.9}$$

is a quarter period of the cosine curve, where it is assumed that $\lambda_0 \approx (\lambda_1+\lambda_2)/2$. In the case shown in Figure 3-2(a), the probing laser at λ_1 yields the maximum sensor sensitivity while the one at λ_2 gives the minimum zero sensitivity. Because the detection sensitivity is also a function of the cavity length d, when the cavity length varies, the detection sensitivities change accordingly. However, at least one wavelength gives sensitivity better than 0.707 of the maximum sensitivity provided $|d-d'| << d$ is satisfied. In the sensing system, signals corresponding to different lasers can be separated by a fixed optical filter and the signal with larger amplitude will be used. The worst sensitivity of the system occurs at the cavity lengths where the two wavelengths give equal sensitivity as shown in Figure 3-2(b).

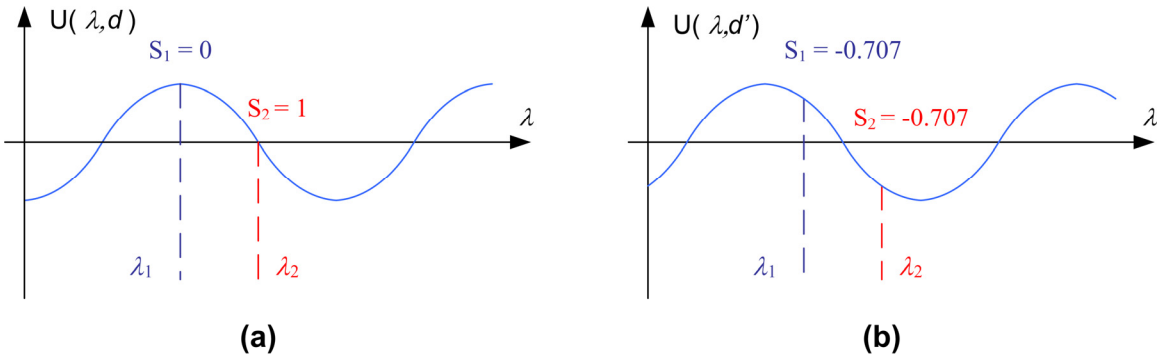

(a) (b)

Figure 3-2: Tow-wavelength quadrature detection at (a) the best condition; (b) the worst condition.

Compared with the traditional *Q*-point control methods which involve tunable lasers or tunable optical filters, two-wavelength demodulation significantly reduced the total system cost. In addition, the stability and robustness is greatly increased without moving parts involved. Moreover, the optical power of the lasers is more efficiently used than tunable filter-based *Q*-point control in which only a small part of the light is used as the probe light.

Note that we have assumed that $|d - d'| << d$ in the above discussions. In such a case, the two wavelengths remain to be quadrature during the cavity length shift. However, when the environment induced sensor cavity length change is so large that the approximation of $|d - d'| << d$ is no longer valid, the original two wavelengths may depart from being quadrature. In such a case, the worst-scenario sensitivity of the system may be reduced. In the following discussion, we calculate the cavity length range that the system can maintain a specific sensitivity.

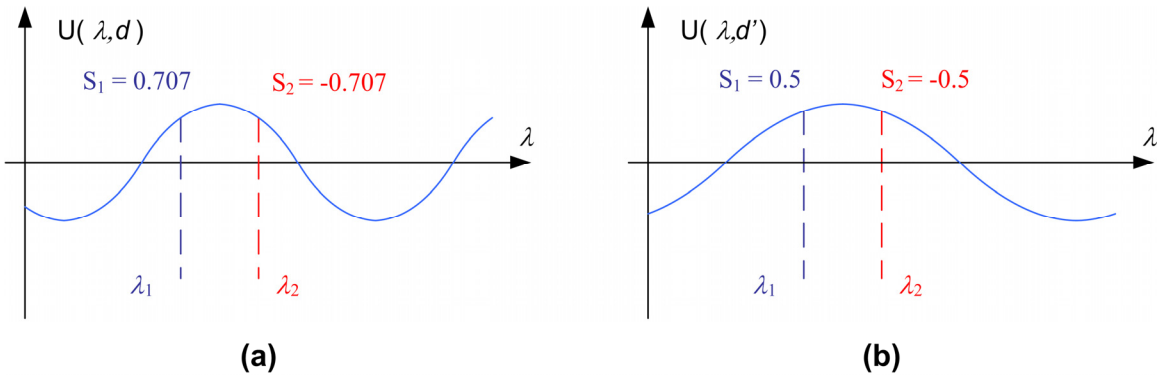

(a) (b)

Figure 3-3: Two-wavelength quadrature detection at (a) the worst condition without background pressure; (b) the worst condition with background pressure.

We assume the worst normalized sensitivity is decreased from 0.707 to 0.5 due to the

increase of the period of the spectral response of the FP sensor, as shown in Figure 3-3. In the condition shown in Figure 3-3 (b), similar to Eq.(3.9), we have

$$\delta\lambda = \lambda_2 - \lambda_1 = \frac{\Lambda'_d}{6} = \frac{\lambda_0^2}{12d'}, \tag{3.10}$$

where Λ'_d and d' are the changed fringe period and sensor cavity length respectively. Eq.(3.9) and Eq.(3.10) lead to

$$\frac{d'}{d} = \frac{\lambda_d}{\lambda_d'} = \frac{2}{3}, \tag{3.11}$$

which indicates that the static-pressure-induced cavity length change must be smaller than 1/3 of the original cavity-length to guarantee the sensitivity is better than 0.5. Therefore, for a highly sensitive diaphragm-based PD sensor, a longer cavity length should be used. A longer cavity length, however, gives smaller $\delta\lambda$ as indicated in Eq.(3.9) and Eq.(3.10), which requires a faster roll-off separation filter to separate the two laser wavelengths. Typically the CWDM add/drop multiplexer has 20dB attenuation at 7nm away from the center wavelength (the central wavelength λ_0 is 1550nm for our system). Therefore, from Eq.(3.9), the maximum cavity length due to this requirement is

$$d_{\max} = \frac{\lambda^2}{8 \cdot \delta\lambda} = \frac{1550^2}{8 \times 7} = 43\mu\text{m}. \tag{3.12}$$

In order to monitor the cavity length during the sensor fabrication, we need at least one fringe (one period: λ_d) inside the spectral measurement window of the component test system (CTS Si720 made by Micron Optics), which covers a spectral range of 50 nm centered at λ_0 = 1545nm. From Eq.(3.8) the minimum cavity length is given by

$$d_{\min} = \frac{\lambda_0^2}{2\Lambda_d} = \frac{1545^2}{2 \times 50} = 24\mu\text{m}. \tag{3.13}$$

Considering these requirements, we select the cavity length d = 40μm. From Eq. (3.8) the corresponding period of the spectral response Λ_d = 30nm. By using Eq.(3.11), the permitted cavity length change is

$$\Delta d = d' - d = -\frac{d}{3} = -\frac{40}{3} = -13.3\mu\text{m}. \tag{3.14}$$

For the designed PD sensor that has a diaphragm diameter of 1.8mm and thickness of 75μm, the theoretical diaphragm sensitivity is 3.9nm/kPa, therefore, if the background pressure is 1bar, the corresponding cavity length change is only –0.4μm, which is much less than the value given by Eq.(3.14). In this condition, the normalized minimum sensitivity is very close to 0.7.

3.3 Sensor Design Based on Performance Requirements

The basic sensor structure and fabrication procedure have been presented in Section 2.3 and Section 2.4. In this Section the discussion is mainly focused on the sensitivity, the response frequency, and the tolerance for cavity length drifting.

Based on the analysis given by J. Xu, *et al.*[50], the center sensitivity of such a diaphragm based pure silica acoustic sensor is

$$Y_c = 2.524 \times 10^{-6} \frac{a^4}{h^3} (\text{nm/kPa}), \tag{3.15}$$

where a and h are the radius and thickness of the diaphragm in microns respectively. The resonant frequency of the diaphragm is given by

$$f_0 = 2.72 \times 10^6 \frac{h}{a^2} (\text{kHz}) \tag{3.16}$$

By putting those values listed in Table 2-2 into Eq.(3.15) and Eq.(3.16), the sensitivity and the frequency response as functions of the diaphragm thickness are plotted in Figure 2-1. It is evident that there is a trade-off between the sensitivity and resonant frequency in choosing the diaphragm thickness. For the current design, a sensitivity of 3.9nm/kPa and a resonant frequency of 252kHz are calculated, which covers the typical frequency range (20~200kHz) of PD-generated acoustic waves.

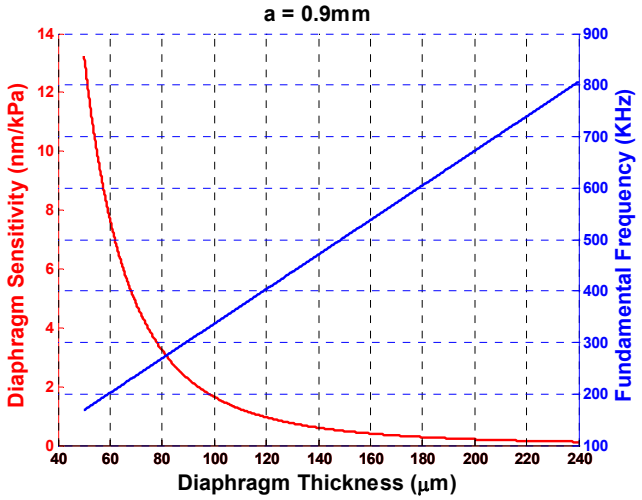

Figure 3-4: Sensitivity and resonant frequency vs. diaphragm thickness.

Note that Eq.(3.15) is only valid when the deflection is less than 30% of the thickness of the diaphragm, the maximum operating pressure is given by

$$P_{\max} = 0.3hY_c^{-1} = 0.3\times 75\times 10^3 \div 3.9 = 5.8\times 10^3 (\text{kPa}), \qquad (3.17)$$

which is much greater than the maximum pressure inside a transformer under normal conditions.

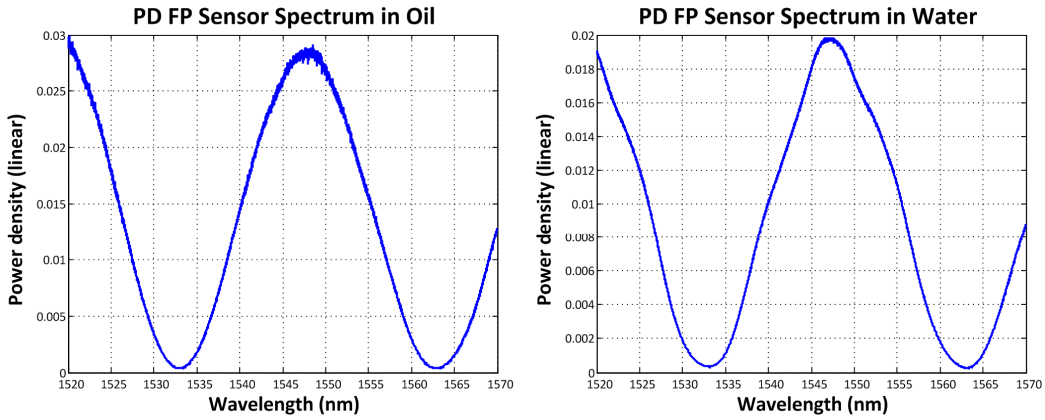

(a) (b)

Figure 3-5: Reflection spectra of a PD FP sensor in (a) transformer oil and in (b) water.

The reflection spectrum of a PD FP sensor is given in Figure 3-5, from which the fringe visibility of this sensor is calculated to be about 96%. The distorted sensor spectrum in water was caused by the outer diaphragm surface reflection induced interference. Since

the refractive index of the transformer oil is very close to that of the fused silica, no anti-reflection treatment to the outer diaphragm surface is needed when the sensor is immersed in oil.

3.4 Single Channel PD Detection

In order to check the efficiency of the quadrature detection, A PD detection module with a single channel (single PD sensor) was built and also a static pressure test bench was built to provide similar pressure environment inside a transformer. The schematic of the PD detection system is shown in Figure 3-6 and a picture of the setup is given by Figure 3-7.

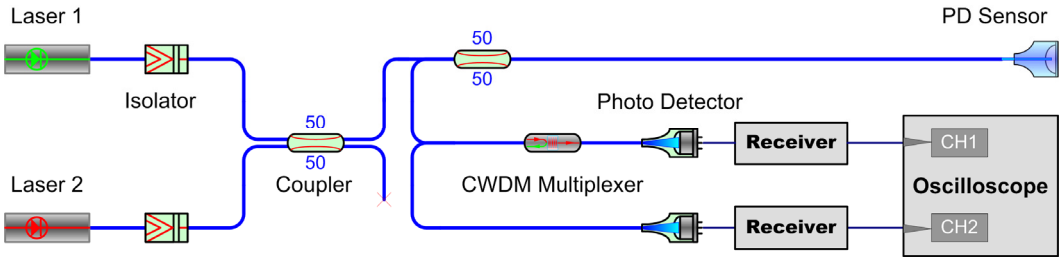

Figure 3-6: Schematic of single channel PD detection system.

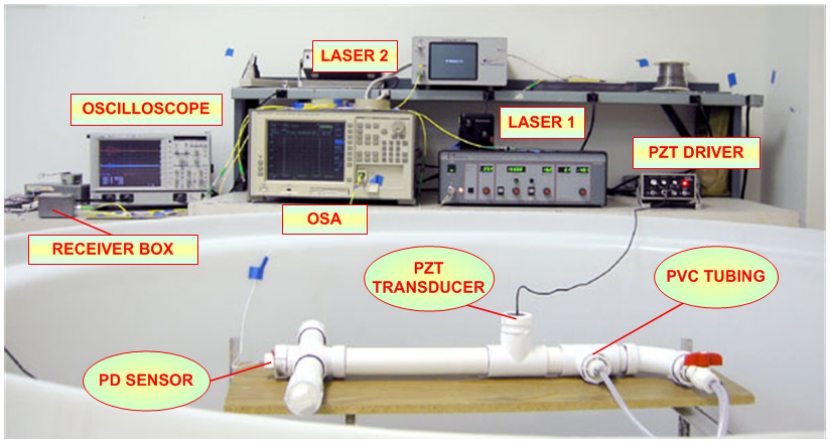

Figure 3-7: Picture of the single channel PD sensor test system.

In the experiment, a fiber optic PD sensor and a PZT for PD simulation were sealed inside a polyvinyl chloride (PVD) tube shown in Figure 3-7. The tube was filled with water and the pressure of the water inside can be adjusted by controlling the valve of a faucet

connected to the tube through a hose. Two tunable lasers were used as Laser 1 and Laser 2 in Figure 3-6 and their wavelengths were set to be 1537.8nm and 1550.3nm respectively. The wavelength difference was chosen to give the worst condition that the normalized sensitivities could be zero in one channel and 0.5 in the other channel. The output powers of the two lasers measured by an optical spectrum analyzer (OSA) were adjusted to be the same. The PD signals were acquired by the oscilloscope at three different pressures: (1) without extra pressure; (2) the pressure which extinguishes the signal of Laser 1; (3) the pressure which extinguishes the signal of Laser 2. At each pressure, signals from both channels and the reflection spectrum of the PD sensor were recorded. Figure 3-8 shows the results corresponding to pressure conditions (1) to (3). It is clear that no matter at what pressure; a strong PD signal was detected either from channel 1 or channel 2, which verifies the feasibility of the two-laser quadrature detection.

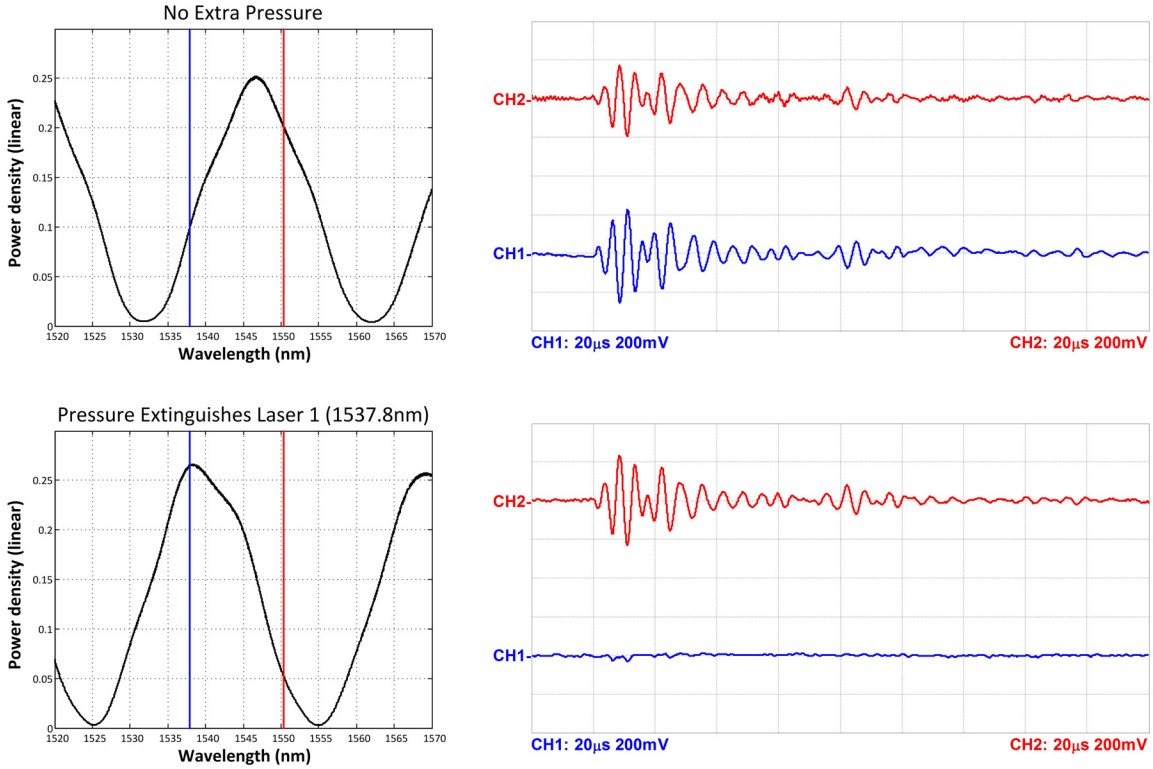

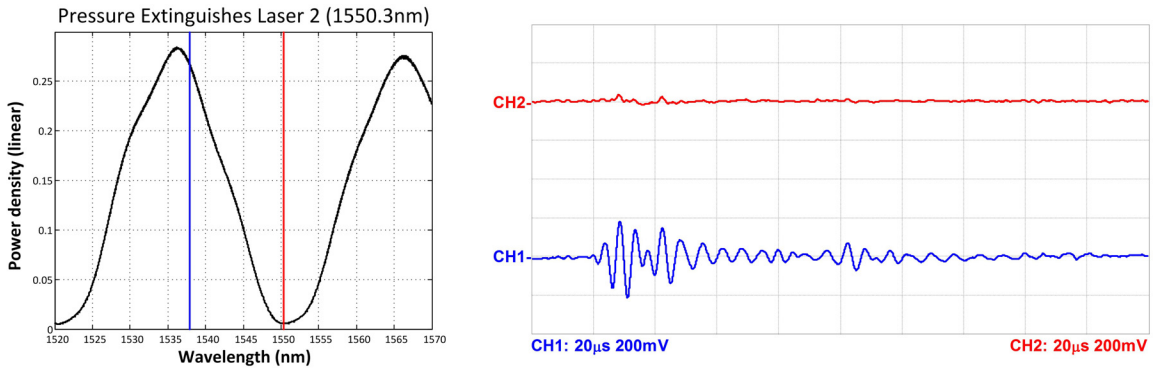

Figure 3-8: Spectra (left) and detected signals (right) from a PD sensor in three conditions.

3.5 4-Channel System Diagram

Figure 3-9 shows the diagram of the multiplexing system with four channels. Light from the Laser 1 and Laser 2 is distributed into the four PD sensors through several stages of 3-dB fiber optic couplers. For each channel of the PD detection, the reflected laser light from the PD sensor is separated by a CWDM add/drop multiplexer; and then an optical receiver with a transimpedance amplifier (TIA) and two bandpass filters is used to convert and amplify the optical signal into AC electric signal. A 4-channel A/D acquisition card is used to convert the analog signal into digital data flow and sent it to the computer. A PC program recognizes and records each PD event.

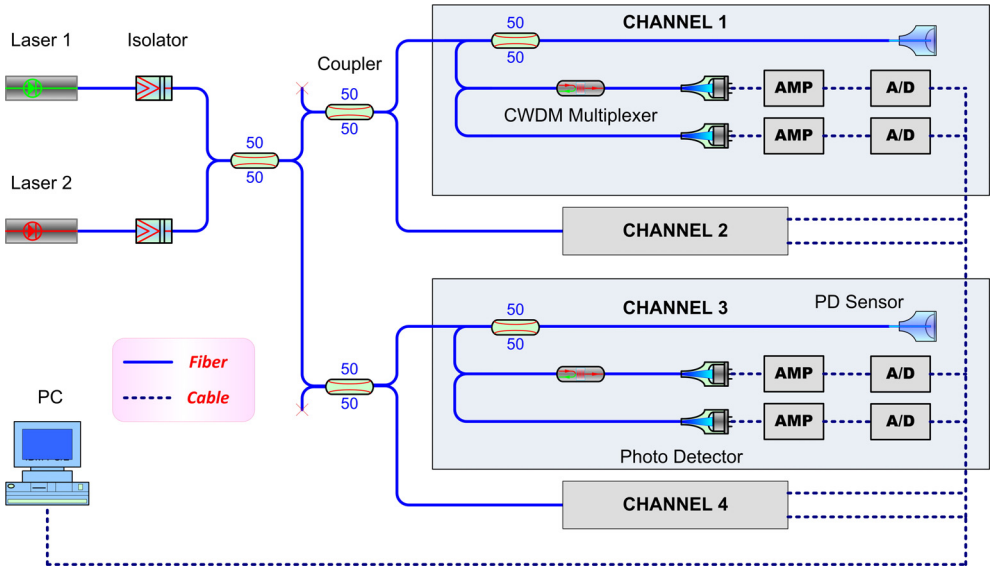

Figure 3-9: Low cost PD sensor multiplexing system with four channels.

3.6 Optical Receiver Box

In the sensor system, a transimpedance amplifier (TIA) was used to transfer and amplify the current generated by a photo detector into voltage. Because the bandwidth of PD acoustic signals is limited, a bandpass filter was put after the TIA to suppress out band noise. Since the gain and noise of the TIA ultimately limit the minimum detectable acoustic signal, this part of circuits needs to be carefully designed. The optical receiver box is composed of 8 identical channels of such a TIA followed by a bandpass filter in each of the channels.

A. Increasing the Gain Bandwidth and Suppressing the Noise

According to the research of transimpedance amplifier designs[51, 52], an effective way to increase the signal to noise ratio (SNR) of a TIA is to increase the negative feedback resistor as large as possible. The reason is that, although the feedback resistor generates thermal noise, the noise level is proportional to the square root of the resistance, R, meanwhile the gain of the amplifier is proportional to R, therefore the SNR is proportional to the $\sqrt{R}$. Since the gain bandwidth product (GBP) of an op-amp is a constant, the final key is to find a high bandwidth and low noise op-amp and to increase the feedback resistor until the bandwidth meets the lowest requirement of the application. The stray capacitance of a large resistor also limits the bandwidth of a TIA. A smart way to decrease the effect of the stray capacitance is to put large resistors in series, because capacitance decreases when capacitors are in series, but the equivalent resistance increases. Another issue which limits the gain of the TIA is the coupling mode of the photo diode to the amplifier. Usually a photo diode is connected to the amplifier with DC coupling, but the DC component in the light signal from the EFPI sensor is 40,000 times of the sensed acoustic signal, so the TIA can be easily saturated by this DC component even under a moderate gain. Therefore, we changed the coupling mode from DC to AC. Before a real PCB board was made , the circuits of the amplifier and the bandpass filter were simulated using Tina-TI. Figure 3-10 shows the simulation circuit, in which an OPA657 and a 1.6GHz low noise operational amplifier were used and the feedback consisted of five 2.2 MΩ resistors in series. The receiver response is given in Figure 3-11

and the in band electronic noise was calculated to be 630 μV.

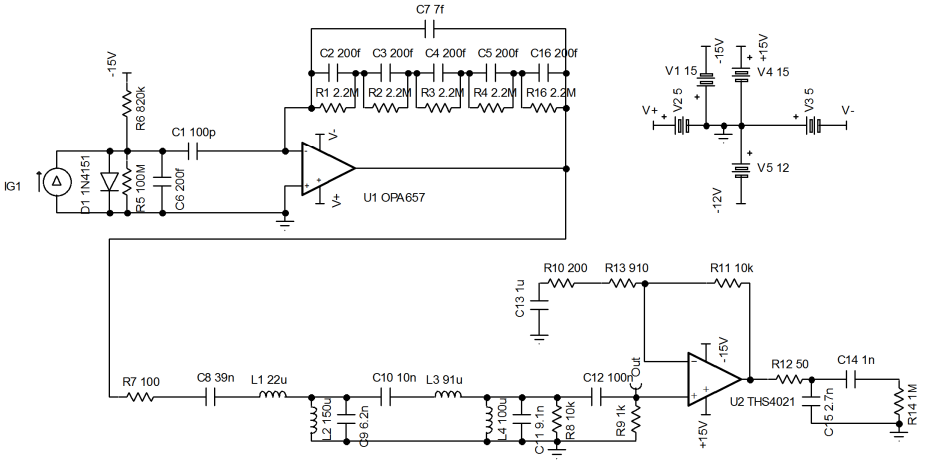

Figure 3-10: Transimpedance amplifier and band pass filter circuits for simulation.

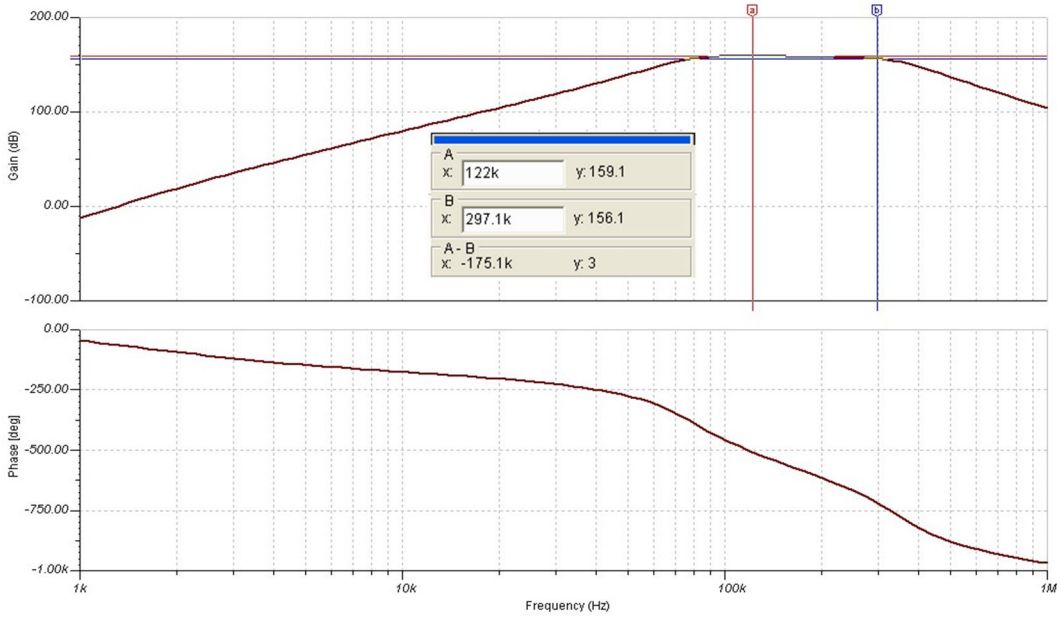

Figure 3-11: Frequency response of the simulated optical receiver.

B. Optical Receiver PCB Fabrication

An eight-channel optical receiver circuit was designed and the PCB was fabricated. Figure 3-12 shows the single channel circuit and a picture of the etched receiver PCB is shown in Figure 3-13(a). Because the current A/D card only supports 4 channels of input, only 4 channels on the board were used. Figure 3-13(b) shows a picture of the finished

receiver box.

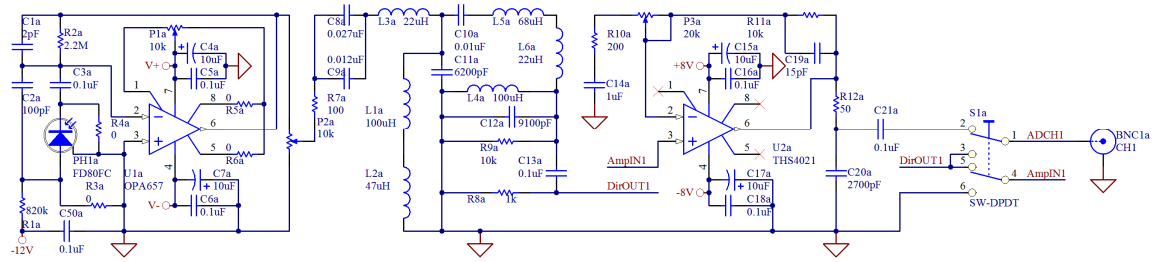

Figure 3-12: Single channel receiver circuit.

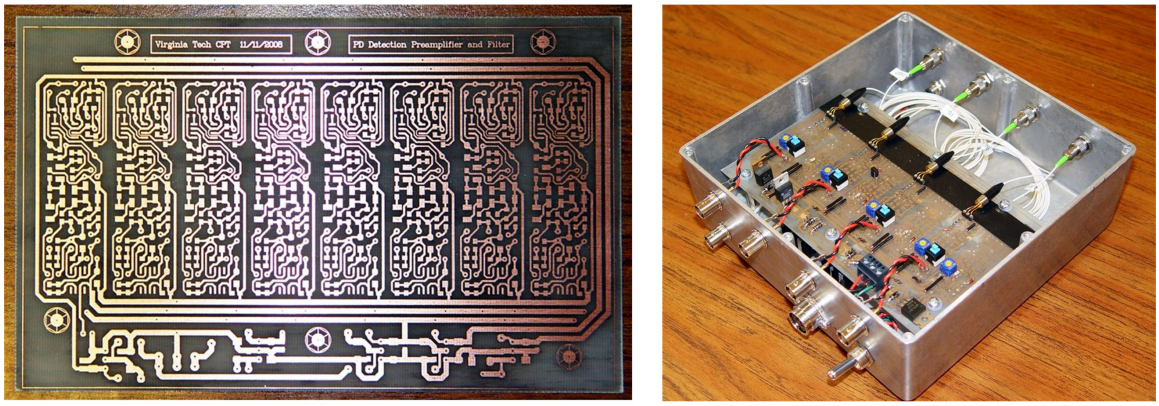

(a) (b)

Figure 3-13: (a) Etched PCB of the 8-channel receiver; (b) receiver box after assembly.

C. Performance of the Receiver

The feedback resistor was finalized as three 5.1 MΩ resisters in series and the 3 dB pass band of the receiver was measured to be from 75 kHz to 310 kHz using a function generator and an optical amplitude modulator. Figure 3-14 and Figure 3-15 show the electronic noise of the new and old receiver (made by a previous researcher at the CPT), respectively and in Table 3-1 the performance of these two receivers are compared. The gain of the new receiver is 2 times as that of the old one and the total electronic noise of the new receiver is 1/3 of that of the old one. It is worthy to mention that, as shown in Table 3-1, the performance of the new receiver is one magnitude better (when bandwidth is considered) than that of the SR570 low noise current amplifier, an active product of Stanford Research System, Inc.

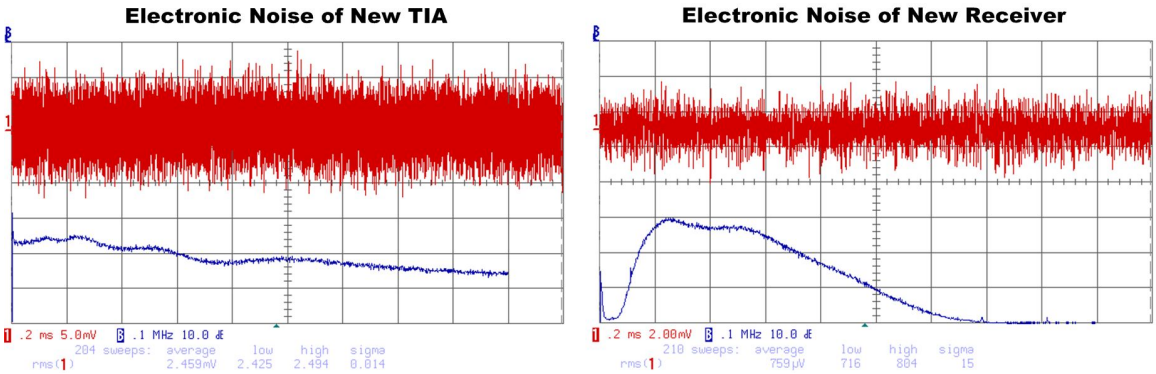

Figure 3-14: Noise performance of the new TIA and receiver.

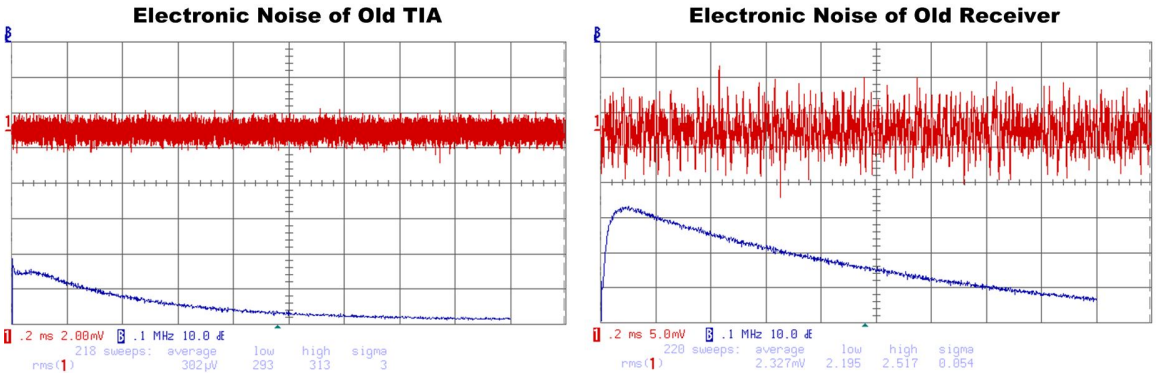

Figure 3-15: Noise performance of the old TIA and receiver.

Table 3-1: Receiver performance comparison

Receiver Type	Lower Cutoff (kHz)	Higher Cutoff (kHz)	Bandwidth (kHz)	TIA Noise (mV)	Receiver Noise (mV)	TIA Gain (V/A)	Receiver Current Noise (fA/√Hz)	Receiver Gain (V/A)
New	75	310	235	2.46	0.76	1.5×10^{7}	160	1×10^{8}
Old	12	220	208	0.30	2.33	2×10^{5}	32000	5×10^{6}
SR570 Low Noise			2				100	1×10^{7}
SR570 High Bandwidth			20				600	1×10^{7}

3.7 Laser Source Design

In order to decrease the system cost and minimize the size of the system, a double laser diode driver chip, FL500, was used and its peripheral circuits were modified from the chip application notes. One important change is we substituted the switching DC/DC regulator with two linear regulators. Although this change made the driver a little bulky, the power noise was decreased dramatically. Controlled by this driver, the two lasers can operate either in constant current mode or in constant power mode, and the driving current and laser power can also be easily monitored and controlled. The two lasers were mounted on one aluminum block which helps keep their temperature relatively stable, and thereby keep their laser lines relatively stable. Figure 3-16(a) and (b) show the etched PCB and the assembled laser source box after assembly, respectively.

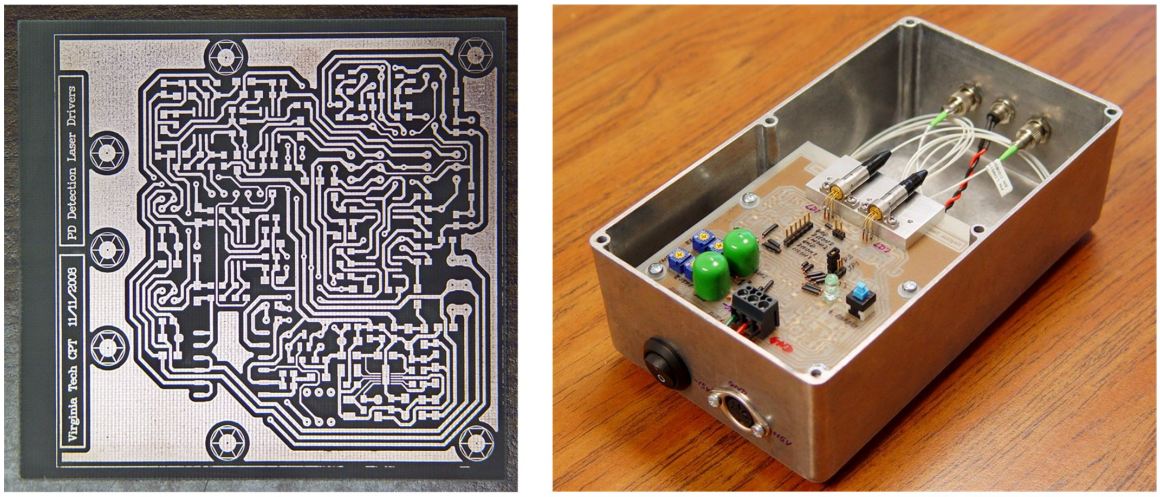

(a) (b)

Figure 3-16: (a) Etched laser driver PCB; (b) laser source box after assembly.

The intensity noise of the lasers were measured by connecting the laser to the optical receiver through a variable optical attenuator (VOA), and adjusting the laser intensity arrived at the detector to be the same as that from the sensor head. As shown in Figure 3-17, the noise was 8mV, which was much larger than the electronic noise of the receiver.

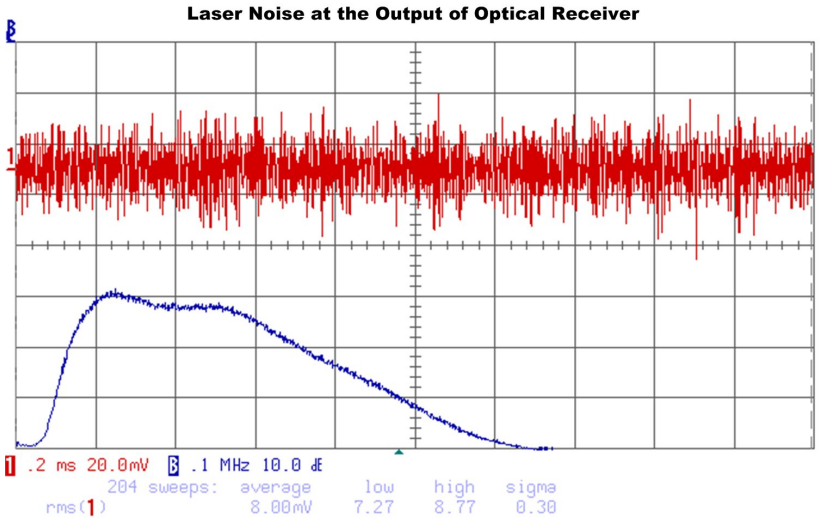

Figure 3-17: Laser intensity noise at the output of the optical receiver.

3.8 PD Signal Processing Box

As shown in Figure 3-18(a), for simplicity and reliability purpose, all the fiber optic components, such as circulators and filters, were mounted on an aluminum board. And all the optic connections between these components and to the outputs of the laser source box and inputs of optical receiver box were made by FC/APC connectors to eliminate unnecessary reflections.

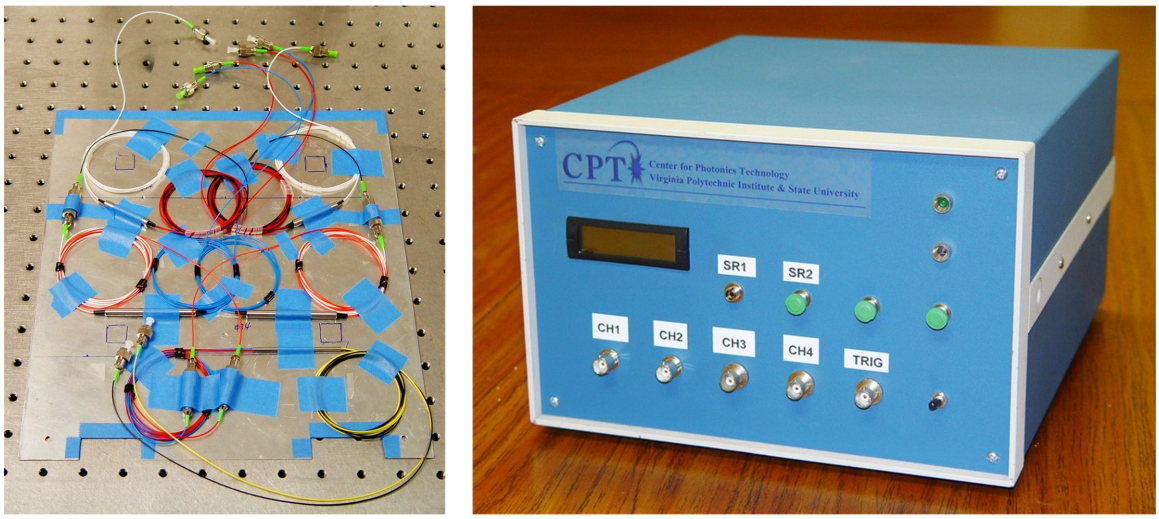

(a) (b)

Figure 3-18: (a) Assembly of fiber optic components; (b) PD signal processing box.

All the modules, including the laser source box, the optical receiver box, the fiber optic components board having passed their performance test, and an additional power regulator were mounted into an aluminum instrumental box shown in Figure 3-18(b) to build the PD signal processing instrument. Because the data acquisition card we used only had 4 channels, two PD fiber optic sensor channels are activated in the instrument.

3.9 Data Acquisition Card and PC Program of PD Event Logging

The data acquisition card, PCI DAS4020/12, used in our sensor system is able to support 4 A/D channels simultaneously sampling at 10 MS/s with 12-bit accuracy, which is quite adequate for sampling PD signals below 300 kHz. It should be the most desirable way if the PC can search PD events in the 4-channel data stream and take records. But the performance of the poor PC we had did not allow this task to be executed in real time. Therefore the circuit in the optical receiver box was modified to generate an assistant trigger signal when PD events occurred and the computer worked in the triggering and recording mode.

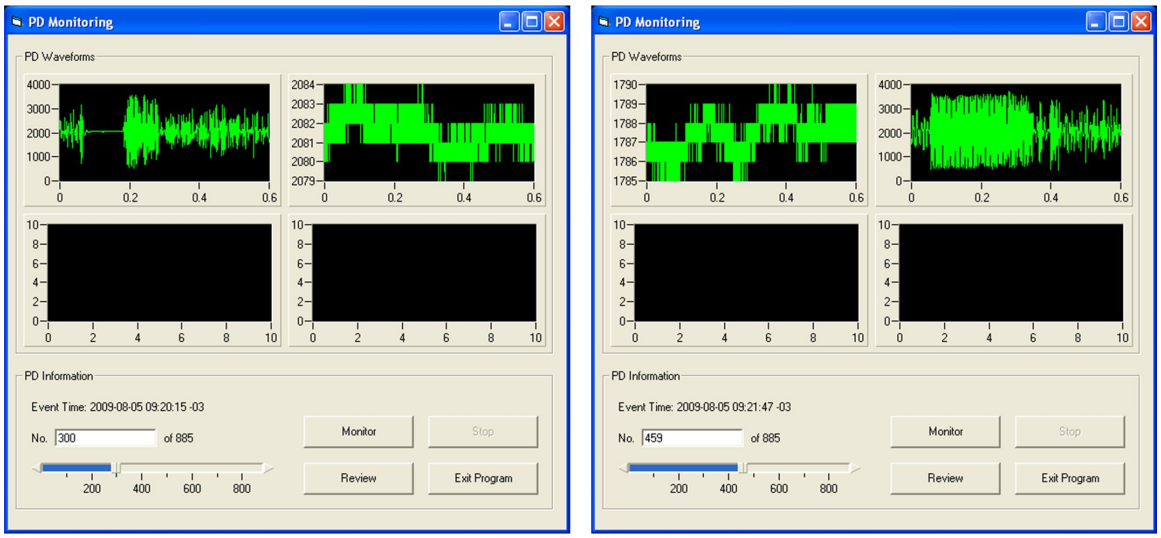

Figure 3-19: User interface of the PD event logging program. (a) Laser1 got signal; (b) Laser2 got signal.

The A/D card control and PD event logging program was written in Visual Basic. When the

program starts, it initializes the A/D card, and sets the card to work in a single trigger mode. When a trigger signal is valid, the A/D card converts and records a certain length of data around the trigger signal, and the PC reads data from the A/D, resets the trigger of the card, finds the PD event stores the PD waveform, displays the event and writes the event to a log file. This procedure will be repeated forever until someone presses the "Stop" button in the program window. The recorded PD waveforms can be easily reviewed when the program is running in the "Review" mode. The user interface of the program is shown in Figure 3-19. As shown in Figure 3-19, only one PD sensor is connected to the system and the upper two plot windows show the signal from the probing Laser1 and Laser2 separately. Figure 3-19(a) shows the situation that Laser1 sees the PD signal and Figure 3-19(b) shows the opposite situation, which illustrates the mechanism of quadrature detection. The PD events shown in Figure 3-19 were recorded in 2009 during a demonstration at the Electric Power Research Institute (EPRI) in Charlotte, NC. There is a prerequisite for the current event logging system, which is that the events should not continuously occur in 3 seconds, which is the period for the PC to save the current data. But a PC with better performance can run this task independently even without the trigger signal.

CHAPTER 4

Detecting Hydrogen Dissolved in Transformer Oil Inside Power Transformers

In order to catch every critical suspicious signal inside a transformer, such as rapid transformer gas concentration variation and abnormal PD activities, people start to pay more attention on the development of on-line real time transformer monitoring systems. Those rapid developing faults can easily be omitted by the traditional periodic examination methods, such laboratory dissolved gas analysis (DGA). However the attacks to a transformer from this kind of faults are usually fatal. As presented in Chapter 2 and 3, an on-line fiber optic PD acoustic sensor system was built and its great advantage is that these fiber optic PD acoustic sensors can be installed inside high voltage transformers to monitor PD activities at the actual locale in real time. To make the fateful decision on a transformer, however, the transformer asset manager still mainly relies on DGA information, because DGA of transformer is always the single best indicator of a transformer's overall condition since its debut in the 1960s. To overcome the the relatively long sampling period of the current laboratory DGA, nowadays, on-line DGA system becomes more popular and it is even reported that some on-line DGA tools offer better accuracy and repeatability than laboratory DGA.

Although current on-line DGA systems can be installed on site and access the transformer oil with a connection port, they can only be installed outside of the transformers and the cost is still high. Known as being capable of detecting a large variety of physical and chemical parameters, compact size and EMI immune, fiber optic gas sensors which can be installed inside transformers and provide real-time DGA will indubitably offer an attractive method for real-time, on-line transformer health monitoring.

4.1 Background of Hydrogen Detection

Hydrogen is becoming a vital clean energy source alternative to fossil fuels. Therefore hydrogen detection becomes an active research area recently. A flourish of research has been carried out for hydrogen detection and many schemes, either optical or electrical, have been developed. However, these methods usually have much limited sensitivities. Most of the sensing schemes have only been tested under hydrogen concentrations higher than 1%. Because of the low sensitivity, their applications in transformers are limited. In power transformers, hydrogen concentration is such an important indicator of their health state that some on-line DGA systems even only monitor the hydrogen concentration. Usually for normally operating transformers, the upper concentration limit for hydrogen in transformer oil is 100ppm. However, it is still beneficial for us to get an overview on all of these methods because new ideas usually root in old ones. Generally speaking, methods of hydrogen detection can simply grouped into three main categories as calorimetric, palladium expansion and chromatographic detection.

A. Calorimetric Method

The first commercial available hydrogen sensor was based on the calorimetric method, and the sensor was called pellister, which was developed at the Health and Safety Executive laboratories in Sheffield, UK. It consists of a catalytic surface constructed around a temperature sensor, and a heater which maintains the catalyst at a sufficiently high temperature to ensure rapid combustion of any flammable gas molecules present. Originally, a platinum coil was embedded in a refractory bead of porous alumina working as both a heater and a resistant temperature sensor. The working temperature usually is around 500°C. Precious metals, such as palladium is defused into the porous alumina bead. The sensor detects gas concentrations by monitoring changes in the resistance of the wire resulting from temperature increases produced by combustion [53]. Generally the sensor has cross sensitivity to any combustible gases and its measurement range is approximately 0.05 to 5% volumetric concentration. With the help of MEMS technology, the sensitivity of this kind of sensor has been improved because a MEMS structure can achieve extremely small heat capacity. Sensors with thermal sensitivity of 5°C/mW were reported in 1995, and their hydrogen detection sensitivity is 3.75°C/1000ppm [54]. A

variation of this kind of calorimetric method is the thermoelectric method, which, instead of using resistance, uses the thermoelectric feature of semiconductors to measure combustion induced temperature change [55-58]. Moreover by using a certain catalyst compound, such as Pt/NiO/alumina, the cross sensitivity is dramatically improved [59]. Generally, this kind of sensors measures the temperature increment caused by catalytic combustion of hydrogen and oxygen and relies on the selection of catalyst to avoid cross sensitivity. For the environment where there is no oxygen and multiple combustible gases coexist, such as sealed transformers, their measurement tends to be inaccurate.

B. Palladium Expansion Method

Palladium is such a special metal that at room temperature it can absorb 900 times its own volume of hydrogen and expand about 10% ~ 30 % in volume[60]. Under conditions with a low hydrogen to palladium ratio, around or less than 0.03 at room temperature, the hydride palladium is all in α phase, expected strain levels are of the order of 3.4×10^{-7} /Pa (H_2) [61]. Since this number is not very large, optical fiber sensors are usually used to measure this small mechanical variance. Examples include fiber Bragg grating sensors [61, 62], EFPI sensors [63, 64] and the MZI sensors [65]. Beside the mechanical expansion, hydrogen absorption also varies the optical properties of a palladium film, such as reflection [66, 67], transmission [68] or refractive index [69-72], and all of them can be used for hydrogen detection. However, the detection lower limits for most of these techniques are above 0.1% and the 100ppm hydrogen detection still relies on large palladium sensing element with a length around 50mm[73], for which temperature compensation becomes very critical. Moreover, the sensitivity of pure palladium hydrogen sensors dramatically decrease with the coexistence of CO or H_2O, known as "poisoning"[74]. Although it can be improved by the silver or gold alloy of palladium, sensors based on these alloys suffer from lower sensitivity and longer response time. Since CO and H_2O also exist in transformer oil, cautions should be taken when a palladium sensor is considered for dissolved hydrogen detection in transformers.

C. Chromatographic Method

Chromatographic method is widely used in traditional lab DGA processes and portable DGA equipment and the standard procedures can be found in ASTM D3612-02. Firstly,

the dissolved gases are subtracted from the sample oil by a carrier gas; secondly the gas mixture is forced to pass a column which is made from a bunch of capillary tubings. Because different gas has different absorbability to the column, they arrive at the out port of the column at different time. A thermal conductivity sensor or a flame ionization sensor is used to detect the amount of arrived gas to get a gas concentration versus time plot. By comparing the measured data with the standard gases timing plot, which determines the species of the gases, the concentration of dissolved gases is acquired. This method is very accurate and sensitive, but it cannot be implemented inside transformers because of its complexity and gas cavity.

4.2 Dissolved Hydrogen Detection Based on Hydrogen Induced Fiber Loss

In the gaseous state, due to the lack of dipole moment, the hydrogen molecule has no strong infrared absorption. However, once the hydrogen molecules diffuse into a silica optical fiber, they are trapped into the glass molecular network and polarized locally, which gives rise to infrared absorption [75]. The fundamental absorption peak locates at 2.42 μm, corresponding to the hydrogen stretching vibration in such a state. There are a number of other peaks which are considered to be the combinations of the hydrogen stretching vibration and the hydrogen rotational vibration or the combination of the hydrogen stretching vibration and the SiO_4 lattice [75].

The fiber optic loss due to hydrogen diffusion has been extensively studied in 1980's for the concerns in the early long-haul fiber-optic communication systems where the hydrogen gas can be generated due to electrolytic corrosion of iron and aluminum metals contained in the optical fiber cable. However, this hydrogen-induced fiber loss has never been exploited for hydrogen detection. One good thing for hydrogen sensing is that the fiber loss induced by hydrogen molecules is reversible so the loss peaks diminishes after the hydrogen-loaded fiber is laid in a hydrogen-free environment.

If this phenomenon can be used for hydrogen detection, the sensor structure will be very simple because only a spool of fiber is needed. Furthermore, the sensor is born to be

suitable for high voltage applications.

Table 4-1 lists the calculated fiber loss at three possible absorption lines for different hydrogen concentrations [76, 77]. It is obvious that detection at 1.88μm gives the best the signal-to-noise ratio (SNR). Due to the lack of a spectrometer that is cost effective and compact for this wavelength, the absorption line at 1.24μm is chosen for our sensor design. Some preliminary experiments were conducted for the 1000 to 1700nm range to examine the feasibility of this method.

Table 4-1: Fiber Loss at Possible Absorption Lines for Different Hydrogen Concentration.

Wavelength (μm)	Fiber loss w/o H_2 (dB/km)	Fiber loss increase for 1bar H_2 (dB/km)	Fiber loss variation at 50ppm H2
1.24	~0.8	~8	~0.003dB (0.1%) @10km
1.88	~2.5	150~200	~0.09dB (2%)@10km
2.42	~1800	~3500	~0.0009dB(0.02%) @10km

4.3 Test of the Sensing Concept and Experiment Results

The first experiment was done at 23°C, and the purpose was to test the response time. Ninety meters of 100/140μm graded index multimode fiber (MMF) was winded on an aluminum spool with a 4 inch diameter and a 1.5 inch height. The transmission spectrum of the winded fiber illuminated by a halogen lamp is shown in Figure 4-1.

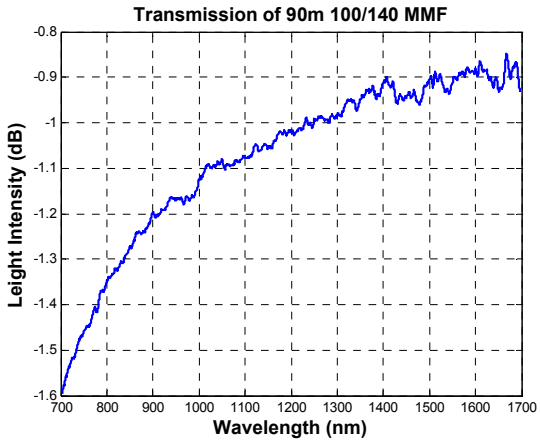

Figure 4-1: Transmission spectrum of 90m 100/140 Multimode Fiber.

The fiber spool was put in a stainless vessel. The vessel was then vacuumed and pressurized with hydrogen up to 21bar at 23°C for 26.5 hours. After the fiber was taken out, we continuously measured the transmission spectrum for 380 hours. Figure 4-2shows the pictures of the hydrogen loading system.

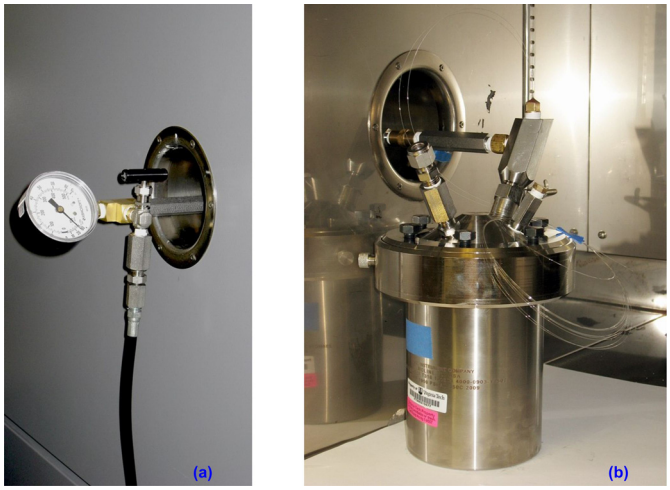

Figure 4-2: Hydrogen loading system. (a) pressure gauge; (b) stainless vessel inside an environmental chamber.

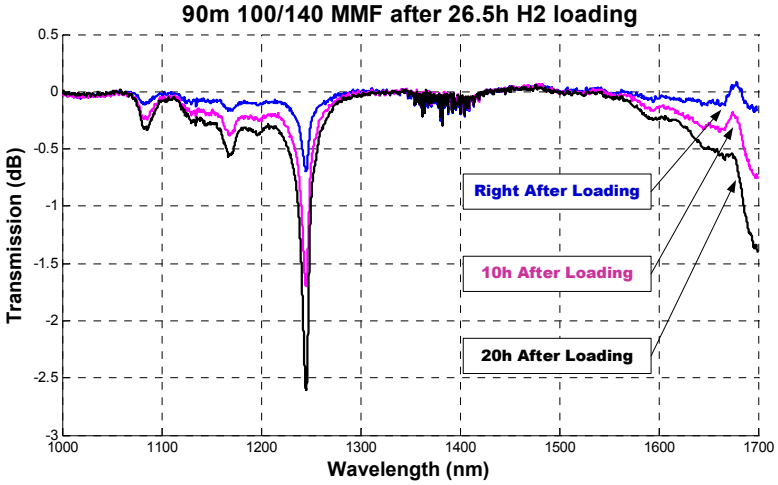

Figure 4-3: Normalized Transmission of 90m 100/140 Multimode Fiber after 26.5h Hydrogen Loading.

It can be seen in Figure 4-3 that within the 1000 to 1300nm range, there are three obvious dips, and their center wavelengths are 1083.6, 1168.5 and 1245.3nm, respectively, which are consistent with the result given by K. Mochizuki, *et al*[75]. There should be another dip around 1700nm but because of the limitation of our light source and spectrometer,

only part of it was observed.

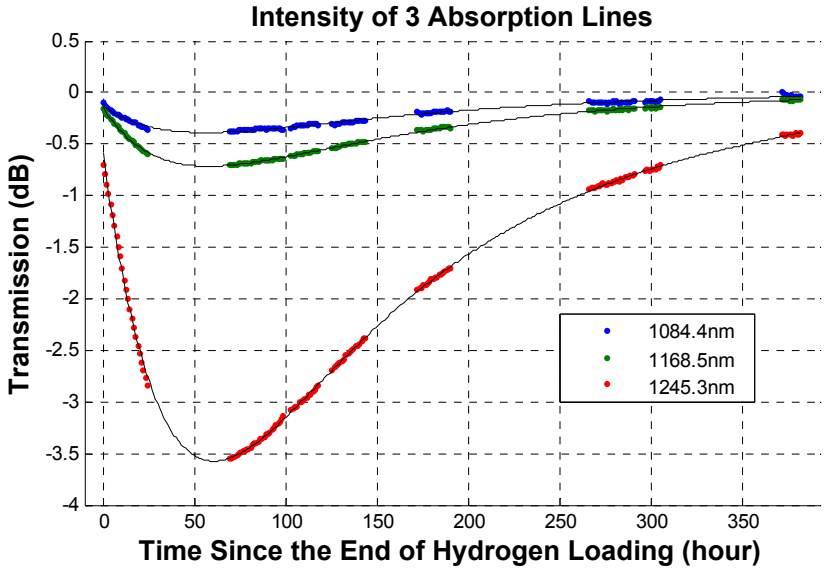

Figure 4-4: Variation of Absorption Valleys versus Time.

Figure 4-4 shows the variation of the three absorption valleys versus time after the hydrogen loading. The interesting thing is that the absorption kept increasing after the loading ended. It may be due to that part of the dissolved hydrogen kept diffusing towards the fiber core after the loading. The maximum absorption of the strongest line at 1245.3nm is 3.6dB and its 80% fully recovery time is around 240 hours, which complies with the result in [78]. The length of the fiber can be easily increased to enhance the detection sensitivity. Also given the slow response which is 10 days at 23°C, improvement is definitely needed to shorten the response time.

4.4 Response Time Analysis

Since the solution of hydrogen in fused silica was treated as small molecules interstitially diffusing through the glass network structure [79], which had been confirmed by its Raman spectrum and the ortho-para conversion of H_2 in optical fibers at low temperatures[80], it follows Fick's laws. For an infinitely long circular cylinder, which is an excellent approximation for an optical fiber, if it has zero initial concentration and its surface is maintained at concentration C_0, for time $t>0$, the concentration distribution at

radial position r is[81, 82]

$$C(r,t) = C_0\left[1-2\sum_{n=1}^{\infty}\frac{J_0(r\xi_n/b)}{\xi_n J_1(\xi_n)}e^{-\xi_n^2\frac{Dt}{b^2}}\right] = C_0\left[1-\sum_{n=1}^{\infty}B_n J_0(r\xi_n/b)e^{-\xi_n^2\frac{Dt}{b^2}}\right] \tag{4.1}$$

where $B_n \equiv 2/[\xi_n J_1(\xi_n)]$, b is the radius of the cylinder, D is the diffusion constant, J_0 and J_1 are the zero and first orders of the Bessel function of the first kind, respectively, and ξ_n, n=1, 2, …, are the roots of

$$J_0(\xi) = 0. \tag{4.2}$$

The hydrogen diffusion constant D is a function of temperature T as

$$D(T) = D_0 T e^{-\frac{E}{RT}} \tag{4.3}$$

where $D_0 = 2.03\times10^{-7}\,\mathrm{cm}^2/(\mathrm{s}\cdot\mathrm{K})$ represents the temperature-independent diffusion constant, E=8.83×10^{3}cal/mol is the temperature independent activation energy for the diffusion process, and R=1.987cal/(mol·K) denotes the gas constant [83].

If we assume that the increase in the fiber attenuation caused by hydrogen depends linearly on the integration of the product of the concentration $C(r,t)$ and the propagating light intensity $I(r)$ over the cross-section of the fiber [77], the increased attenuation over time may be expressed as

$$\Delta\alpha(t) = \Gamma 2\pi\int_0^b C(r,t)I(r)rdr\,, \tag{4.4}$$

where Γ is a measure of the sensitivity of attenuation to concentration. Applying Gaussian approximation to the single mode fiber electric field distribution we have

$$I(r) = I_0 e^{-2r^2/w^2},\ (r<b)\,, \tag{4.5}$$

where w is the mode filed radius, I_0 is the light intensity at the center of the fiber. For Corning SMF28e, at 1310nm, w=4.5μm and b=62.5μm. Substituting Eq.(4.1) and Eq.(4.5) in to Eq.(4.4) yields

$$\Delta\alpha(t) = I_0 \Gamma 2\pi C_0 \left(\frac{w^2}{4} - \sum_{n=1}^{\infty} B_n e^{-\xi_n^2 \frac{Dt}{b^2}} \int_0^b J_0\left(r\xi_n / b\right) e^{-2r^2/w^2} r dr \right) \tag{4.6}$$

By extending the upper limit of the integration to infinity and using the Equation 11.4.29 in Ref.[84] namely

$$\int_0^{\infty} e^{-a^2 t^2} t^{\nu+1} J_\nu(bt) dt = \frac{b^\nu}{(2a^2)^{\nu+1}} e^{-\frac{b^2}{4a^2}} \quad (\Re\nu > -1, \Re a^2 > 0), \tag{4.7}$$

with v=0 in Eq.(4.6), the normalized fiber attenuation increase over t is

$$\overline{A}(t) = \frac{\Delta\alpha(t)}{\Delta\alpha_0} \approx \left[1 - \sum_{n=1}^{\infty} B_n e^{-\xi_n^2 \frac{Dt_d}{b^2}} \right], \tag{4.8}$$

where $\Delta\alpha_0 = I_0 \Gamma \pi w^2 C_0 / 2$ is the increase in attenuation after diffusion equilibrium and $t_d = [t + w^2/(8D)]$. For graded-index multimode fiber (GINMMF) with core radius a, if the index distribution is parabolic, the light intensity distribution is given by[78]

$$I(r) = I_0(1 - r^2/a^2), \quad (r < a). \tag{4.9}$$

Similarly, by substituting Eq.(4.9) to Eq.(4.4) the normalized fiber attenuation increase over t is

$$\overline{A}(t) = \frac{\Delta\alpha(t)}{\Delta\alpha_0} \approx \left[1 - \sum_{n=1}^{\infty} B_n' e^{-\xi_n^2 \frac{Dt}{b^2}} \right], \tag{4.10}$$

where $B_n' \equiv 16b^2 J_2(\xi_n a / b) / [a^2 \xi_n^3 J_1(\xi_n)]$.

4.5 Sensor Response Time Improvement

Based on the relations given by Eqs.(4.3), (4.8) and (4.10), it is obvious that the response time for this detection method can be shortened by either increasing the detection temperature T or decreasing the fiber diameter b. Since in typical power transformers the operation temperature is about 80°C. For single mode fiber SMF28e, which is widely used in the fiber communication industry, the minimum possible diameter is 30μm

without a substantial loss increase. Simulation results are depicted in Figure 4-5. Promisingly, the calculated 80% response time for the 100/140 MMF at 80°C has been dropped to 18 hours.

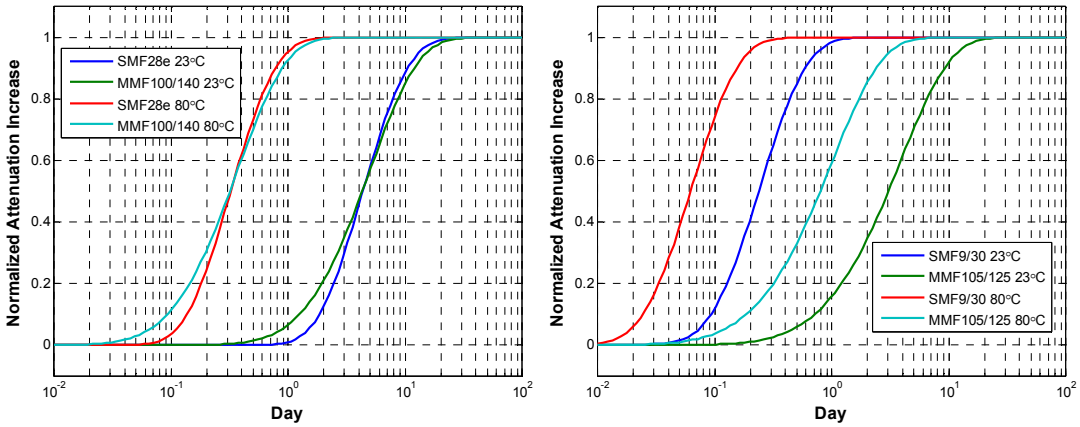

Figure 4-5: Normalized hydrogen induced attenuation response.

In order to prove this estimation, we ran another experiment at 80°C and at this time, 200kPa hydrogen was filled in the vessel and the measured fiber transmission variations at three absorption wavelengths are shown in Figure 4-6. As expected, the diffusion process became much faster at 80°C and the 80% response time decreased to 13 hours, which is even faster than the theoretical estimation. The absorption at 1.24μm is 1.5dB for 90m MMF put in 2bar hydrogen, which corresponds to 8.4dB/(km·bar), so it meets the 8dB/(km·bar) theoretical value well.

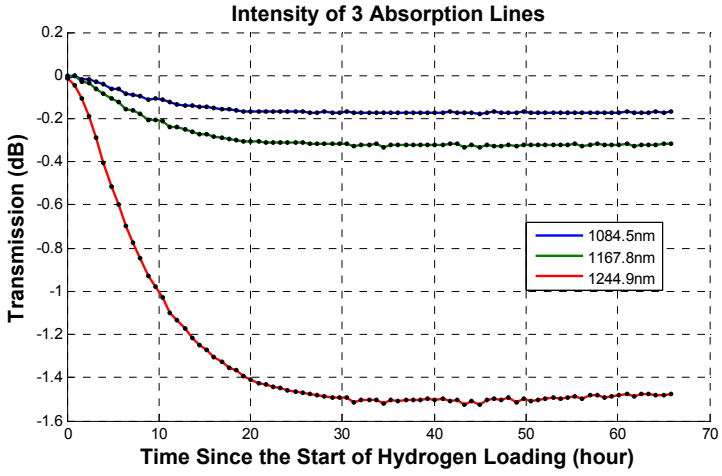

Figure 4-6: Variation of absorption valleys versus time in 200kPa hydrogen.

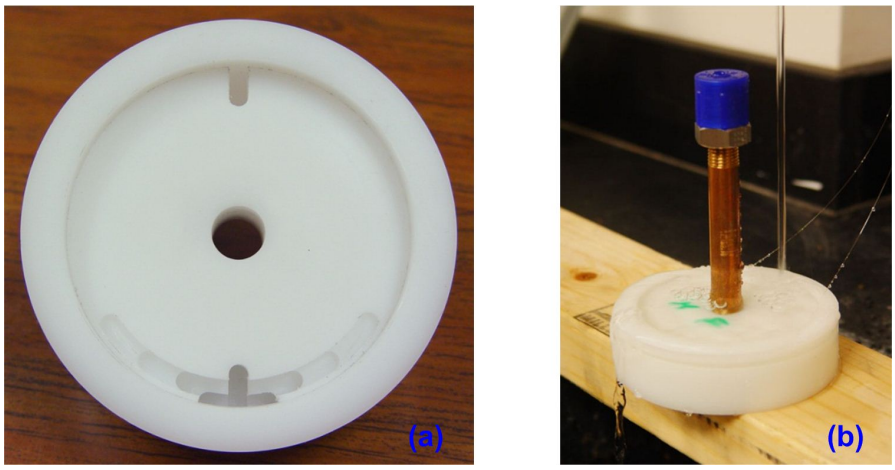

Figure 4-7: (a) The machined fiber etching box; (b) fiber rinse after etching.

To further enhance the response rate, a smaller diameter fiber is indispensable, but this kind of fibers is rare and expensive. In order to run a quick test a fiber etching box (shown in Figure 4-7) was designed and machined with high-density polyethylene, with which the diameter of a standard SMF28e fiber was etched down to 32μm. The entire etching process was monitored by a CTS to secure the total fiber loss in the hydrofluoric (HF) acid solution is less than 1dB. Figure 4-8 shows the averaged fiber transmission variation during etch (two samples) and Figure 4-9 illustrates the diameter difference. Typically bare fibers (fibers without protection coating) are fragile, but when the fiber is etched down to 32μm the fiber become rather flexible, which is important for industrial applications.

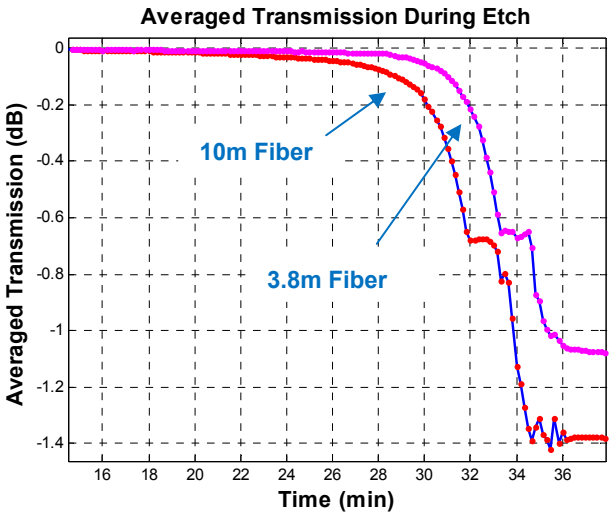

Figure 4-8: Fiber transmission variation during etch.

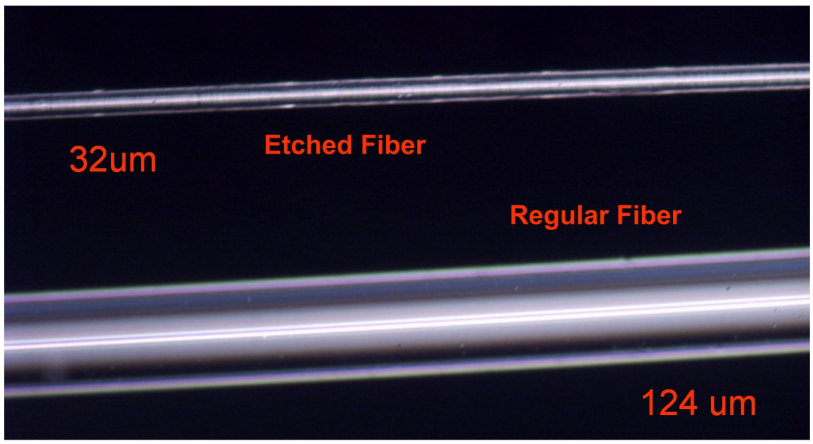

Figure 4-9: Diameter comparison between the regular and etched fibers.

Summarily, six different fiber types or experimental conditions were tested and the results are listed in Table 2-1. D_0 has been adjusted to $2.33\times10^{-7}\,\mathrm{cm}^2/(\mathrm{s}\cdot\mathrm{K})$ for a better match of the experiment results. Although there was difference between the expected fiber response times, which were calculated from the theoretical analysis, and the tested values, smaller fiber diameter and higher test temperature are effective factors to bring the response time close to one hour level. W-index-shaped fibers and capillary tubes, in which the light intensity distribution is closer to the fiber or tube surface, are also possible candidates for faster response rates.

Table 4-2: Measured and calculated 80% response time for different fibers.

Fiber Type (μm)	Length (m)	Temp. (°C)	Response Time	Expected Time
100/140 MMF	90	23	240h	244h
100/140 MMF	90	80	13h	18h
9/125 SMF	30	80	12h	16h
9/70 D-Shaped	30	80	7h	-
9/30 SMF	3.8	50	4h	3h
9/30 SMF	10	80	2h	0.9h
9/30 SMF	-	23	-	12h

4.6 Current Detection Limit

From the theoretical estimation listed in Table 4-1, for 50ppm hydrogen detection, 10km fiber is needed, which is equivalent to detecting 500ppm H_2 with a 1km fiber. Moreover, in the previous section, we only tested the fiber loss with gaseous state of hydrogen, but the results presented here were acquired by putting optical fibers into Voltesso 35, a widely used transformer insulating oil, with hydrogen dissolved.

The hydrogen loading system shown in Figure 4-2was modified for the oil sample test. In order to release the huge pressure increase due to the oil expansion at high temperature, as shown in Figure 4-10, a syringe based bleeding mechanism was added, which both releases the oil pressure in the vessel and keeps hydrogen from leaking out. The first test done with this system was a 5% hydrogen test, which also worked as a system feasibility test.

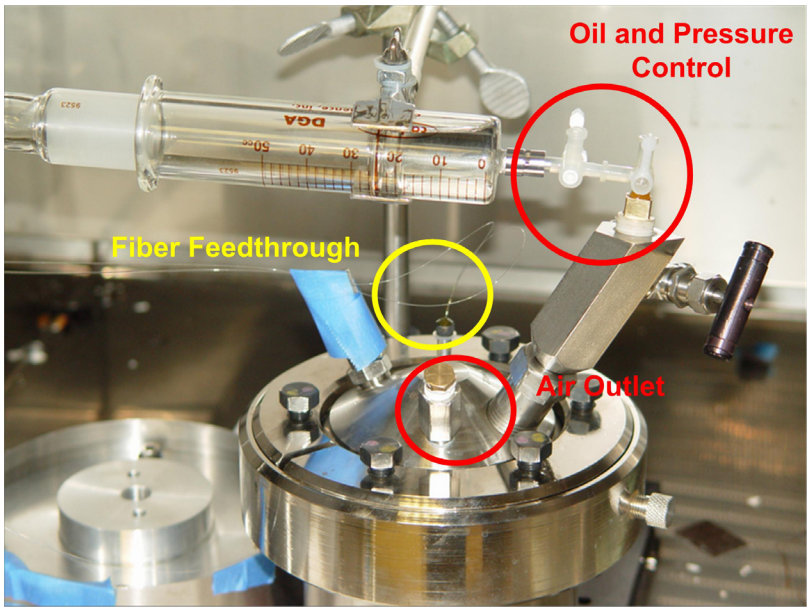

Figure 4-10: Modified hydrogen loading system for oil sample test.

One kilometer single mode fiber (SMF-28) was winded on the 4-inch spool, carefully put in to the 4-inch stainless steel reactor and sealed by six bolts. By following the ASTM guide D3612, 130ml Voltesso 35 was vacuumed for 2 hours and 6.5ml hydrogen at atmospheric pressure was dissolved in it to make the 5% H_2 sample. Then the oil sample was injected to the reactor through the oil and pressure control port. A single mode fiber

(SMF) coupled light-emitting diode (LED) (MRED14C015-FC made by Luminent) centered at 1289nm with 45nm 3dB spectral width served as the light source and an optical spectrum analyzer (OSA), ANDO AQ-6315A, was used to acquire the transmission spectrum of the 1km fiber soaked in the oil with 2nm resolution. Although the LED only coupled 200μW into the single mode fiber, it was still brighter than a halogen lamp in the spectral range of interest and less noisy than a typical super continuum light source. The transmission spectrum of 1000m SMF is shown in the left part of Figure 4-11 and the increase trend of hydrogen induced loss with time can be seen clearly in the right part of Figure 4-11.

Figure 4-12 illustrates the exponentially fitted variation of absorption intensity over time. The measured 80% response time was 12.5 hours and 5% hydrogen induced loss in the 1km SMF was around 1dB, which is 12.5 times of the theoretical value shown in Table 4-1. Right now the reason for this increase is still unknown.

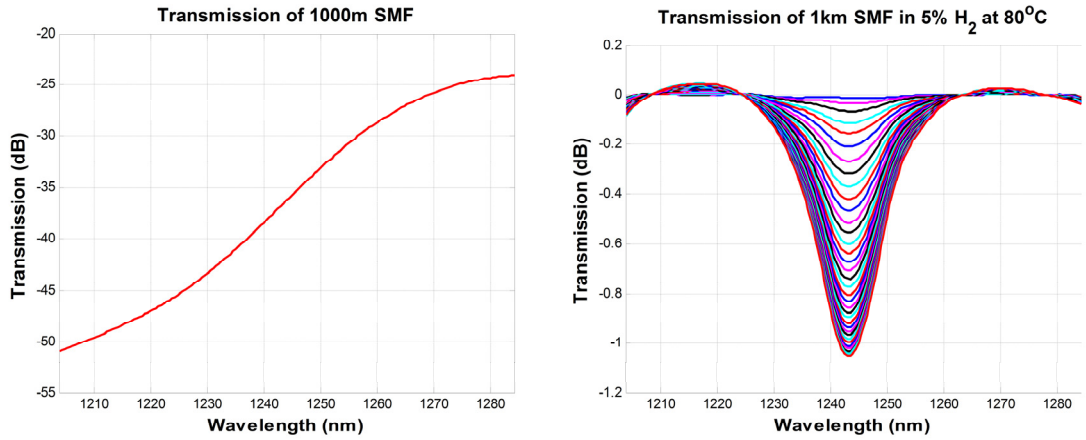

Figure 4-11: Transmission of 1km single mode fiber in oil with 5% H_2.

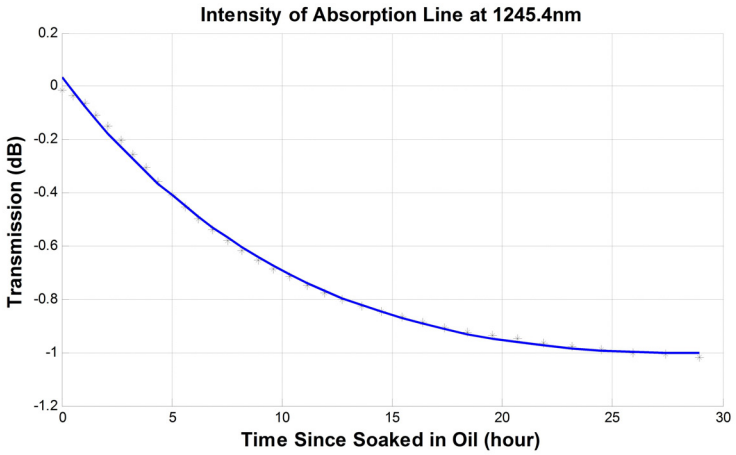

Figure 4-12: Intensity of H_2 induced fiber loss over time.

The second test was conducted using an oil sample with 1000ppm H_2 dissolved. Since the volume of hydrogen, which was only 0.13ml, exceeded the accuracy of our syringe, we prepared some oil with 1% hydrogen and mix this oil with vacuumed oil having a volume ratio of 1:10. But after more than 24 hours test, no absorption was observed. It is believed this method may not be sufficiently accurate. For the 1km fiber detection limit test, we used the True North oil standard made by Morgan Schaffer. The test was run in a 6-inch system.

As shown in Figure 4-13 the 1km SMF fiber was winded on a self-made aluminum spool which also worked as a lid to seal the system with two 4mm width O-rings when it was pushed into the canister. Two vertical screw holes on the spool were used to inject oil in and let air come out, separately. Two tilted screw holes served as the fiber feedthroughs, and they were sealed with a 5min cure epoxy which can survive at 80ºC. After the sealed cavity was filled with oil, these two vertical screw holes were sealed with two 1/4-20 screws. When winded with 1km fiber, the canister was able to hold about 300ml oil. During the test, temperature was kept at 80ºC, which caused the oil to expand and the induced pressure by this expansion was automatically released by the corresponding rising of the fiber spool inside the canister allowed by the O-ring structure.

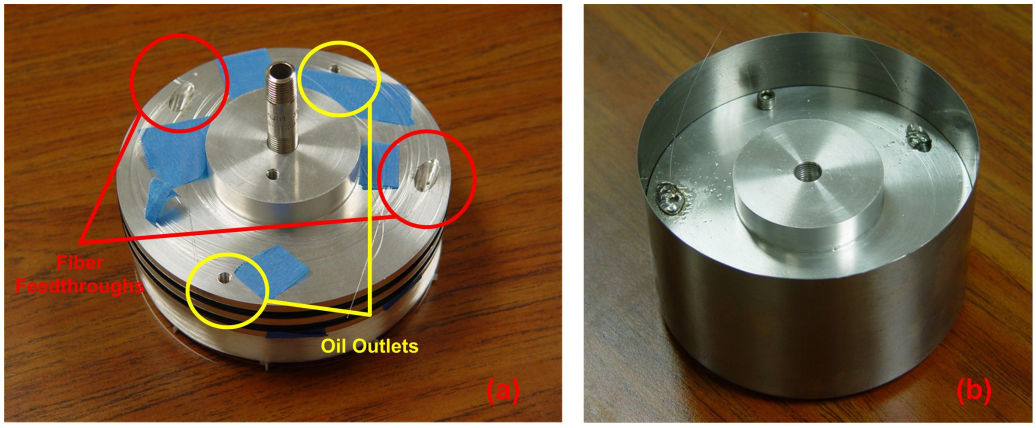

Figure 4-13: (a) 1km fiber winded on the 6-inch aluminum spool; (b) the 6-inch fiber spool sealed in the 6-inch canister.

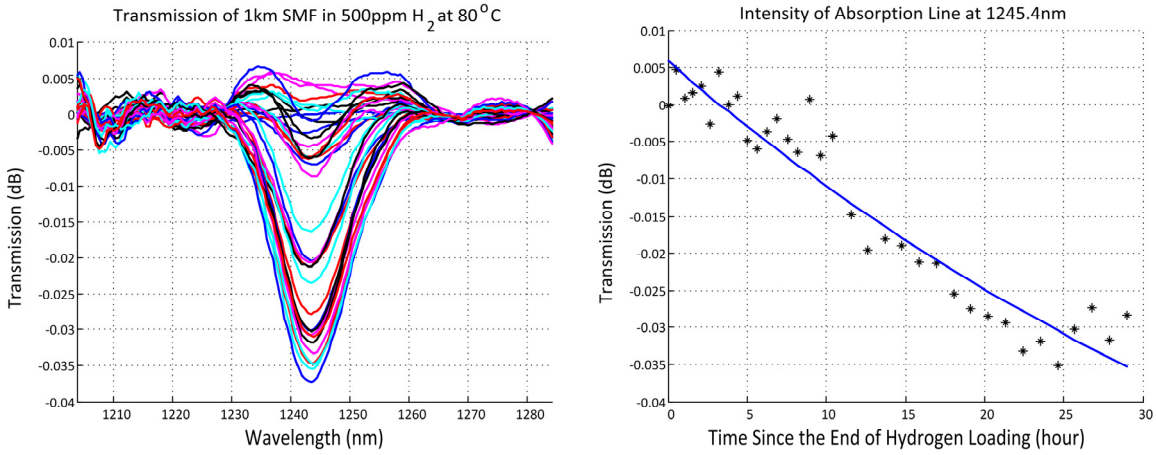

Figure 4-14: Transmission of 100m single mode fiber in oil with 500ppm H_2.

Figure 4-14 shows the results of 500ppm hydrogen detection. It seems the absorption stopped at -0.03dB, which is still around 10 times of the theoretical value. But we believe this is very close to the detection limit of current system.

4.7 Conclusions and Directions for Improvement

By the experimental results it can be clearly seen that the detected hydrogen induced fiber loss is usually 10 times of the theoretical value, which should be further proven by more experiments. We should also consider the dilution of the hydrogen concentration due to the large fiber volume to oil volume ratio. For the current system the hydrogen detection

limit for 1km SMF is better than 500ppm. Since the LED we used is very weak, its power varies more than 25dB over the measurement spectrum range (the left part of Figure 4-11), and the intensity fluctuation was not normalized, there is still pretty large room for further improvement. Currently LEDs centered at 1310nm with 10mW and 80nm 3dB bandwidth are available. By using balanced detection or a second harmonic detection method with a tunable filter, 10 times of sensitivity enhancement should be possible.

CHAPTER 5

Detecting Acetylene Dissolved in Transformer Oil inside Power Transformers

Acetylene is another very important gas in DAG. Since hydrogen is the easiest gas to generate in fault activities, acetylene is the hardest gas to generate, because its production needs much higher energy. Usually when the concentration of acetylene exceeds the limit, which is 5ppm, it indicates arcing or severe overheating inside a transformer.

5.1 Background of Acetylene Detection

Different from hydrogen, acetylene has quite strong absorption lines in the fiber communication spectrum range, so the detectable limit for acetylene is usually very low and even down to ppb level is possible. Generally, methods of acetylene detection can simply be grouped into four main categories as calorimetric, chromatographic, direct absorption intensity measurement and photoacoustic detection. Because the calorimetric and chromatographic methods are very similar to what has been presented in the hydrogen detection chapter, here only the last two methods are elaborated.

A. Direct Absorption Intensity Measurement

Acetylene has more than 40 absorption lines around 1.5μm, which can even be easily observed by a collimated light beam [85, 86]. Optical sensors based on intensity measurement of these absorption lines have been developed and their detection limit can reach 100ppm level without difficulty [87, 88]. By using cavity-enhanced, or ring down techniques the detection limit can even reach 1ppm level [89-91]. All of these methods require the acetylene be in gaseous phase, which is hard to realize inside transformers.

B. Photoacoustic Spectroscopy

Laser photoacoustic (PA) spectroscopy is well recognized as one of the most sensitive gas detection technologies[92]. The photoacoustic effect is based on the conversion of light energy into sound energy by the target gas that needs to be monitored. Its principle of operation is illustrated in Figure 5-1. A laser source is first intensity modulated before it emits into the gas cell. When the light frequency corresponds to a resonant vibration frequency of the gas, some of the light photons will be absorbed. During this process, the gas molecules will be excited to a higher vibration energy state. The higher energy state is not stable; therefore these molecules will subsequently relax back to the initial lower vibration energy state that is stable. The primary relaxation process is non-radiative; that is the energy is transferred to the heat energy of the molecules instead of radiating photons. As a result, the laser absorption causes a temperature and pressure increase. If the laser is modulated at a certain frequency, the temperature and the pressure will be modulated at the same frequency as well. The modulated pressure will then generate a pressure acoustic wave, which can be measured by a microphone installed on the wall of the gas cell. The intensity of the acoustic waves is directly related to the gas concentration in the gas cell.

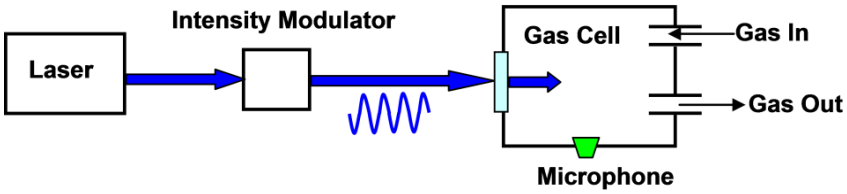

Figure 5-1: Illustration of Laser Photoacoustic Spectroscopy.

Because most gases have the resonant wavelengths that are unique to themselves, the gas detection by the laser photoacoustic spectroscopy is highly selective. This method is particularly suitable for those gases with strong absorption lines at popular laser wavelengths and acetylene perfect example that has strong absorptions at wavelengths around 1550nm. In fact, sensors with detection sensitivity down to ppb level have been demonstrated using this method [93-95].

However, there are limitations when the traditional photoacoutic spectroscopy is used for gas detection inside a transformer. First, the microphones used in traditional photoacoutic

spectroscopy are either condenser microphones or electret microphones. Although highly sensitive, they are electrical sensors and not suitable to be installed inside transformers. Second, traditional photoacoutic spectroscopy can only detect the molecules in the gaseous states so it can not be used in an oil environment. Therefore, for inside transformer detection of acetylene dissolved in transformer oil, a new method is desired.

5.2 First Experiment on Dissolved Acetylene Detection by Direct Oil Transmission Measurement

To our best knowledge, all of the current dissolved gas analysis (DGA) methods need to extract the dissolved gases out of the oil and measure the concentration of these gases in gaseous phase. This is corresponding to the IEEE guide on DGA for transformers, but it is not convenient and cannot give on-line information. We developed a new method, which can get the concentration of dissolved acetylene or other gases by directly measuring the transmission spectrum of the solvent oil. There is one prerequisite for this method that the dissolved material modifies the transmission spectrum of the solvent uniquely. Presently we only proved that this method works for acetylene dissolved in transformer oil, but other transformer gases, such as hydrogen, ethylene, methane, ethane, carbon monoxide, *ect.*, may also have their unique absorption when dissolved in oil or other solvents. The advantage of this method is obvious, the fiber-optic sensing probe which is intrinsically safe and immune to electromagnetic interference (EMI), can be placed inside the transformer for on-line real-time DGA. More accurate and localized dissolved gases information can be detected, which is very useful for transformer health condition monitoring and diagnostics.

Test of the Sensing Concept and Experiment Results

The sensing concept was tested with a flexible setup, which gave the ability to predict the concentration of acetylene dissolved in the transformer oil. As shown in Figure 5-2, two optical collimators were separated by 22cm and aligned with each other. A simple cylindrical cell between the collimators was made from a 146mm plastic glass tube (OD=25mm and ID=20mm) having two microscope glass slides glued to its ends as optical

windows. Two ports, which are named as P1 and P2 in Figure 5-2, were mounted to the cell with a 120˚ angle to facilitate the flow of gas and oil respectively. The cell was mounted on a vertically adjustable stage with a travel distance larger than the diameter of the cell. A Components Test System (CTS) was used to measure the transmission of this system.

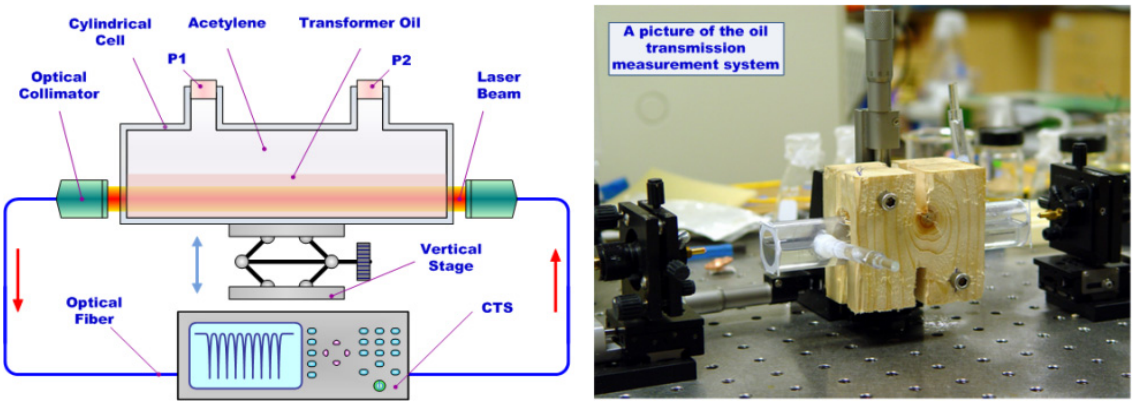

Figure 5-2: Schematic and Picture of the Oil Transmission Measurement System.

At beginning the cell was filled with ambient air and its transmission was calibrated as zero. Then the transmission of standard oil was recorded by filling the cell with standard oil with no acetylene dissolved. After the cell was vacuumed and filled with 100% acetylene, transmission of pure acetylene was recorded. A half volume of oil was then injected from a facing down port and it expelled out a half volume of acetylene from the port facing up, and then the two ports were shut. After shaking the cell for 5 minutes to force the dissolution of acetylene into the oil, the cell was put back on to the vertical stage and the wood holders secured the position repeatability. After staying for still for 15 minutes, the transmission of the gas part was measured and the absorption difference from the pure acetylene represented the concentration of dissolved acetylene in transformer oil. Then we adjusted the vertical stage to make the laser beam pass through the oil part and recorded the transmission. In order to get stable spectrum and minimized the random noise induced by ambient interference, we averaged the measurements for 100 times. Since the sweeping speed of the CTS is 5Hz, it took 20s to get one spectrum which was quick enough for DAG.

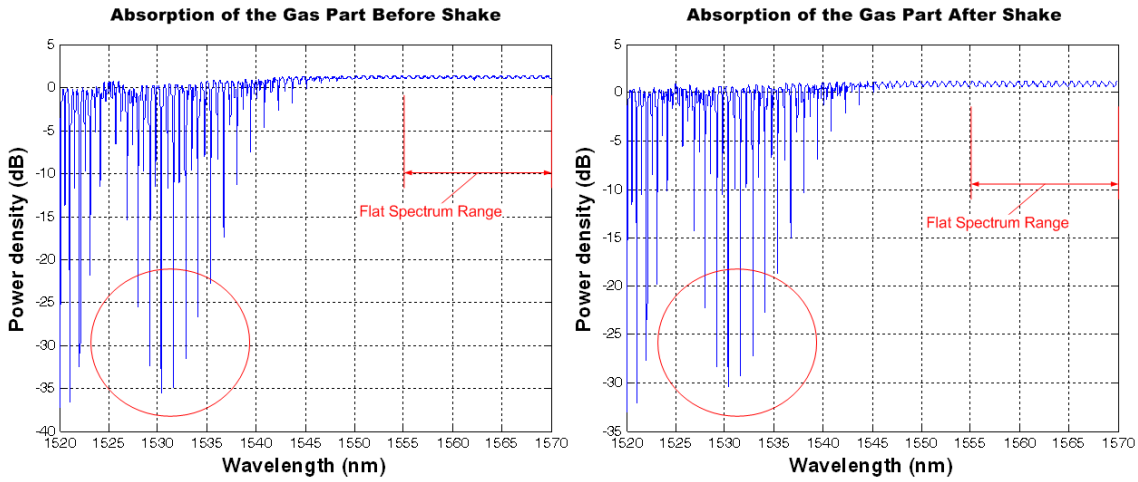

Figure 5-3: Acetylene Absorption in the Gas Part before and after Cell Shake.

Figure 5-3 shows the measured transmission spectra in the gas part before and after cell shake. Because of optical power fluctuation or other unstable factors, the measured spectrum may shift up and down in logarithmic domain, but according to the Beer-Lambert law the only absorption difference between the absorption region and the non-absorption region reflects the absorption intensity. This applies for both the gas phase and oil phase measurements. Since the sweep range for the CTS is from 1520 to 1570nm, we chose the segment from 1560 to 1570 as the non-absorption range and use the average absorption in this range to normalize the measured spectra. It works well for gas phase spectra, but for oil phase ones, because the spectrum in this region is not flat, which means it can only be approximately treated as non-absorption region, some compensation is needed to correct this effect.

After normalization, ten strong acetylene absorption lines were chosen for comparison. A program searched the curve fitted minimum transmission at each absorption line to minimize random noise. Because the amount of acetylene dissolved in the oil part equals the acetylene decrease in the gas part and the gas part and oil part have the same volume, based on the data shown in Figure 5-3, the predicted volume concentration, C, of acetylene dissolved in oil was given by the measurements in the gas phase by

$$C = \frac{I_0(dB) - I(dB)}{I_0(dB)} = \frac{-35 - (-30)}{-35} \approx 14\% \qquad (5.1)$$

where I_0 is the measured absorption line intensity for 100% acetylene, I is the measured absorption intensity for the same line after oil gas mixing, and both I_0 and I are in dB scale.

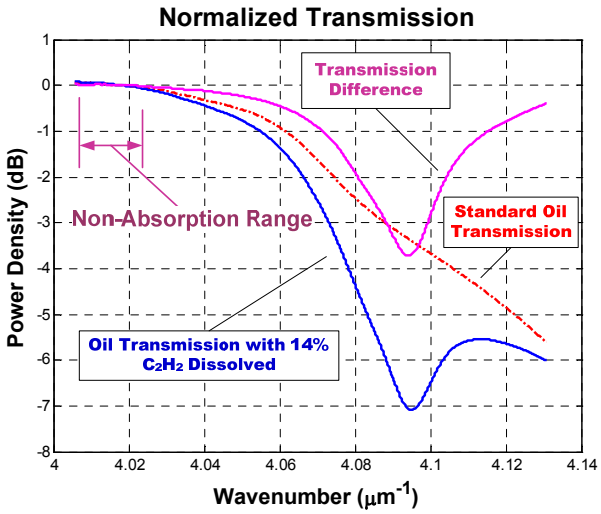

Figure 5-4: Normalized Transmission Spectrum.

Figure 5-4 shows normalized transmission spectra without and with acetylene dissolved inside the transformer oil. Dissolved acetylene produces an absorption dip around wavenumber of 4.095 μm^{-1}, the shape of the absorption dip is quite stable and the depth of the dip is proportional to the concentration of the dissolved acetylene according to both Beer-Lambert law and our test results. Outside the absorption dip region is a wide non-absorption region, and the ratio of the light power at absorption region over that at non-absorption region is a function of the concentration of the dissolved acetylene while is not sensitive to the fluctuation of the source power and transmission loss, so this detection method can be regarded as self-calibrated.

Discussion on the Absorption Spectrum in Oil

Figure 5-5(a) shows the acetylene induced absorption pit over 1460 to 1620nm with oil spectral background removed and Figure 5-5(b) shows the absorption lines of acetylene in gaseous state. Obviously there are four major differences: 1) a series of peaks in the gaseous spectrum become a single broad peak in the oil; 2) the broad peak has a

Lorentzian shape other than a Gaussian one; 3) the center of the broad peak shifts to the longer wavelength relative to the gaseous spectra, which implies frequency decrease; 4) the counterpart of the R-branch in the oil spectrum is missing. Because these phenomena are very close to the hydrogen absorption peak in optical fibers, some discussion in Ref. [96] can be applied here.

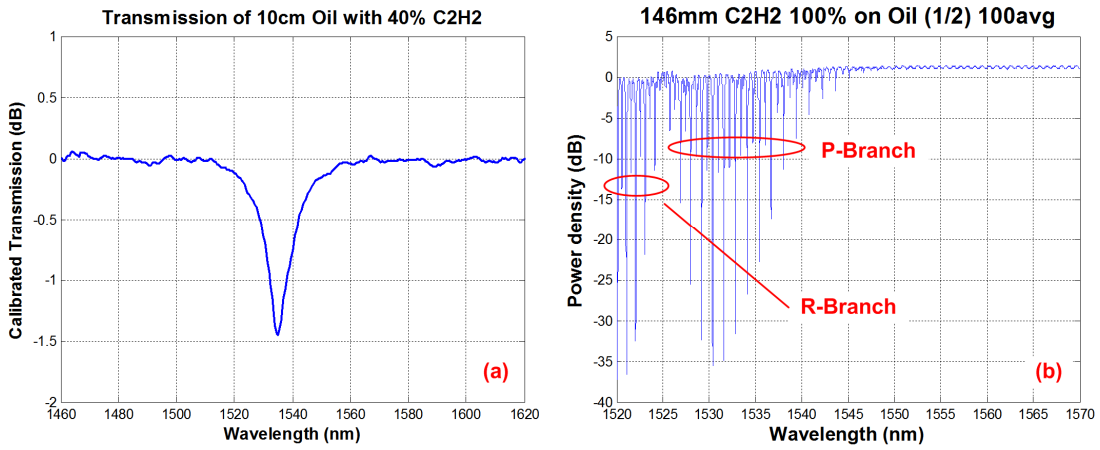

Figure 5-5: (a) C_2H_2 induced spectral absorption pit in oil; (b) C_2H_2 absorption lines in gaseous state.

The similarity between the spectra of dissolved and gaseous molecules implies a physical dissolve other than chemical reaction of acetylene. The small center wavelength shift suggests the small coupling between the C_2H_2 and oil molecules. Since the spectral lines in the P-branch correspond to the vibrational and rotational states of the acetylene molecule, when it is dissolved into the oil, these freedoms of the molecules are restricted and the Lorentzian line shape is an evidence of molecule collision. But the missing of the counterpart in the dissolved spectrum is rather unique. Because the R and P-branches are generated by the two possible dipole moment directions governed by the selection rule, missing of one branch indicates that one dipole moment is restricted. Further research is needed in this direction to explain the details.

5.3 Dissolved Acetylene Concentration Measurement

In order to get the best stability and remove the effect of oil convection caused by probing

laser heating, the oil transmission measurement system, including the two fiber collimators and the cylindrical oil cell, was modified from the original horizontal position, as shown in Figure 5-2, to the vertical position, which is shown in Figure 5-6. Also a standard 100mm quartz cell made by PerkinElmer was used.

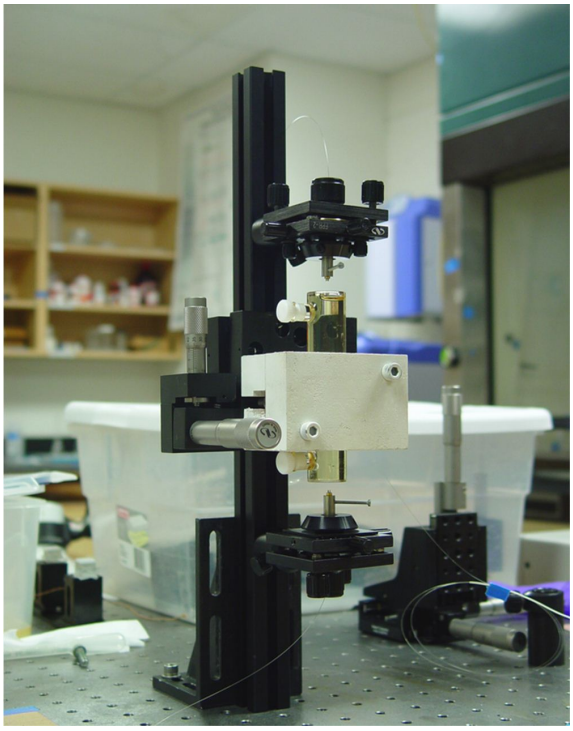

Figure 5-6: Acetylene detection system in vertical position.

According to the Beer-Lambert law, the measured light intensity is

$$I(\lambda, C, t) = I_0 \exp\left[-\alpha(\lambda)L - C(t)\beta(\lambda)L - \gamma(\lambda) + A(t)\right], \qquad (5.2)$$

where I_0 is the input light intensity, $\alpha(\lambda)$ is the oil induced loss, $C(t)$ is the concentration of acetylene, $\beta(\lambda)$ is the normalized acetylene induced loss, $\gamma(\lambda)$ is the loss of the measurement system and A(t) is system loss variation over time (oil aging). Let

$$S(\lambda, C, t) = \ln\left[I(\lambda, C, t)\right], \qquad (5.3)$$

and assume $C(t)$ and A(t) are the only time related variables. Meanwhile $I(\lambda, 0, t_0)$ and $\beta(\lambda)$ are known (which can be acquired by measuring the oil sample with zero and certain concentration of acetylene). We can apply linear curve fitting to the measured

spectrum $S(\lambda,C,t)-S(\lambda,0,t_0)$ with function $\beta(\lambda)L$ as

$$\begin{aligned} S(\lambda,C,t)-S(\lambda,0,t_0) &= A\beta(\lambda)L+B \\ &= -C\beta(\lambda)L+A(t)-A(t_0)\ . \end{aligned} \tag{5.4}$$

Therefore $C=-A$, which is the fitted slope of a straight line. In this process, all the acquired spectral data are used and measurement noise is automatically averaged out by the fitting algorithm.

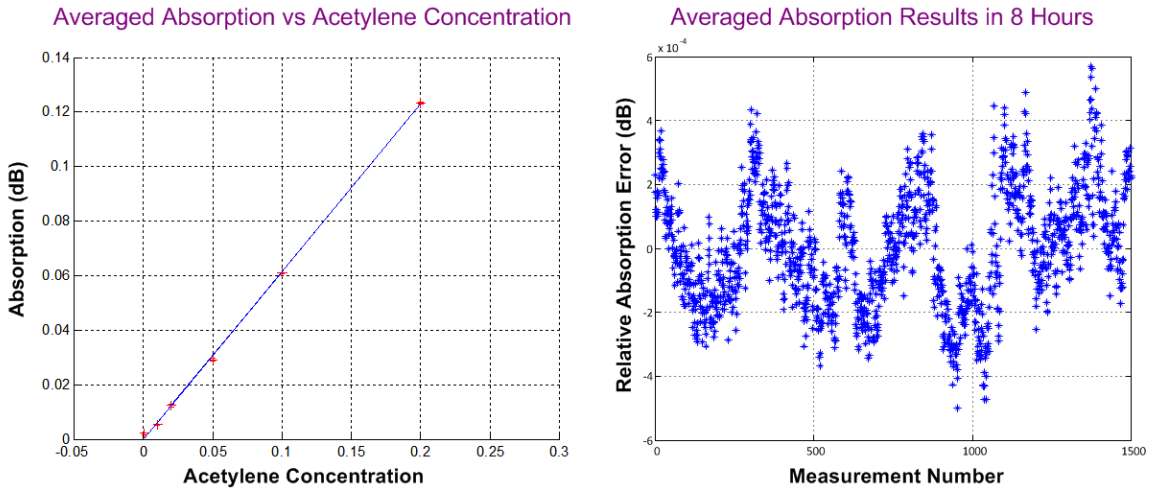

Figure 5-7: (a) Measured absorption vs. acetylene concentration; (b) Relative absorption error over 8 hours.

Based on the algorithm discussed above, six acetylene oil samples with different C_2H_2 concentrations (20%, 10%, 5%, 2% 1%) were measured. Each concentration was measured for five times and the standard deviation is 2‰.

As shown in Figure 5-7(b), 1500 spectra were acquired for the 14% acetylene dissolved oil, which lasted 8 hours, to estimate the resolution of the system. In order to make the results independent of specific light source power, we defined a dimensionless factor e_A and its relation to the measured average absorption A_{avg} and the mean of A_{avg}, A_{mean}, is given by

$$A_{mean} = A_{avg}\left(1-e_A\right) \tag{5.5}$$

Therefore e_A can be calculated from

$$e_A = \frac{A_{mean}-A_{avg}}{A_{avg}} \tag{5.6}$$

Eq.**Error! Reference source not found.** shows the calculated e_A, and the fractional standard deviation of the average absorption (std(A_{avg})/A_{mean})) is 1.8×10^{-4}. Because dissolved acetylene concentration was also measured through the gas part in the cylindrical cell, which was 14%, the short-term detection accuracy of the oil transmission measurement method was 25ppm, and the detection resolution is around 5ppm.

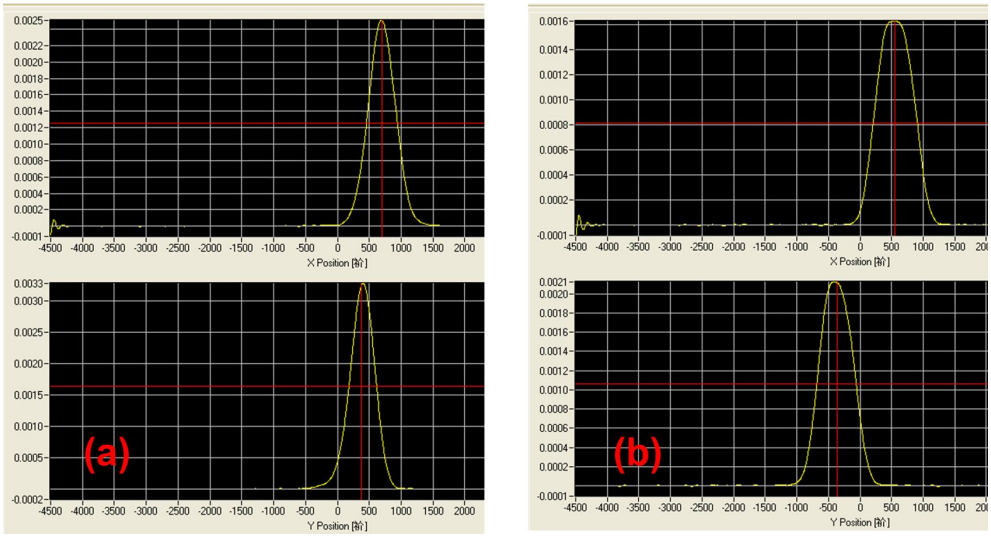

Figure 5-8: Laser beam profiles (a) before the oil cell; (b) after the oil cell.

5.4 Thermal Lens Effect and Photothermal Spectroscopy

During the acetylene concentration measurement, collimator alignment adjustment was indispensable. One interesting thing was that the coupling efficiency through the oil cell was always a little bit higher when one collimator was being adjusted than it was at rest. I order to explain this phenomenon, we measured the laser beam profiles before and after the oil cell and compared them. Obviously, as shown in Figure 5-8, the laser beam became fatter after it passing through the oil cell, which was the reason that the coupling efficiency dropped. Since a small amount of time, around 0.5 second, was needed to build up this deformation, the higher coupling ratio during the collimator adjustment was explained. This observation can be well explained by the photothermal effect.

When a light beam passes through a material, because of the absorption of the material,

some absorbed energy is converted into heat, which heats up the material locally and a temperature profile which is related to the intensity distribution of the light beam is formed. Because usually the refractive index is a function of temperature, a thermally-induced optical lens is generated along the path of the light beam and therefore it varies the power distribution of the beam. If the material is located between two collimators, because of the formation of the thermal lens, optical power coupled into the receiving collimator varies with the absorption of the material. By scanning the wavelength of the input light source, an absorption spectrum is acquired. The time constant of the thermal lens effect is usually on the order of a few seconds and absorption of 10^{-3} to 10^{-4} parts per centimeter are sufficient to produce the effect [97]. Because of its high sensitivity, the thermal lens technique or the photo thermal effect has been successfully used for the absorption spectroscopy of liquids [98, 99].

5.5 System Design and Experimental Setup Optimization for Photothermal Spectroscopy

The schematic of the detection system is shown in Figure 5-9. A tunable diode laser (Newport 6328) worked as the scanning pump laser. In order to cover the entire absorption peak with sufficient margin, the laser was scanned from 1515nm to 1570nm. The laser output was modulated into sinusoidal shape at 100Hz by an optical modulator and the modulation signal was also sent to an oscilloscope as the trigger reference. Because the output power of the tunable laser varied with different wavelength by more than 30%, a 99:1 coupler was added to tap 1% of the source power, which worked as a power reference for normalization purpose. Then the laser was delivered to the cylindrical cell by a collimator. A distributed feedback (DFB) laser with center wavelength at 1573nm worked as the probe laser and it entered the oil cell from the other end. Since the two collimators were aligned the probe laser was coupled back into the fiber through Collimator A. An optical filter at 1573nm with 1nm bandwidth was placed at the output port of the Circulator A to block possible reflected pump laser power. The photo detectors and the transimpedance amplifiers converted optical power to electric signals, which were captured and processed by a digital oscilloscope.

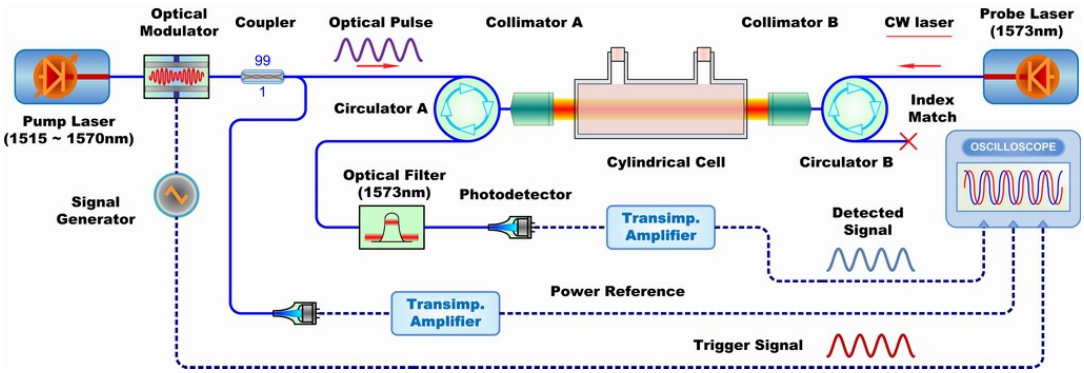

Figure 5-9: Schematic of the photothermal detection system.

At the beginning a 10cm cylindrical cell was used and the cell was mounted on a vertical frame. This construction secured both a long optical path for stronger absorption and the minimum liquid convection because the sensing laser entered the cell from the top. Both of these two factors were critical for transmission loss measurement. But later we found that for photo thermal spectroscopy such a long oil column was not necessary, since the oil absorption was so large, about 1dB/cm, only very small portion of the probe laser could arrive at the Collimator A. So we changed to use a 2cm cell and made another holder which is shown in Figure 5-10. Two graded index lens collimators were held by two 5-axis stages. Because of the compact frame design, system stability was enhanced. Moreover the 2cm cell gave nine times stronger signal than the 10cm cell did.

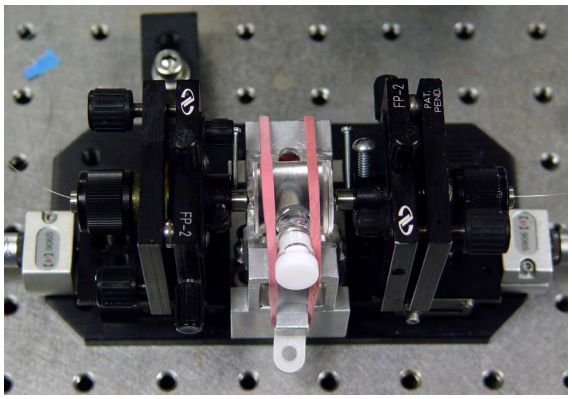

Figure 5-10: Holder for 2cm cylindrical cell with two adjustable collimators.

5.6 Data Acquisition and Processing

Both the pump laser scan and the data acquisition were controlled by a LeCroy 7zi digital oscilloscope. A typical oscilloscope screen shot is given in Figure 5-11.

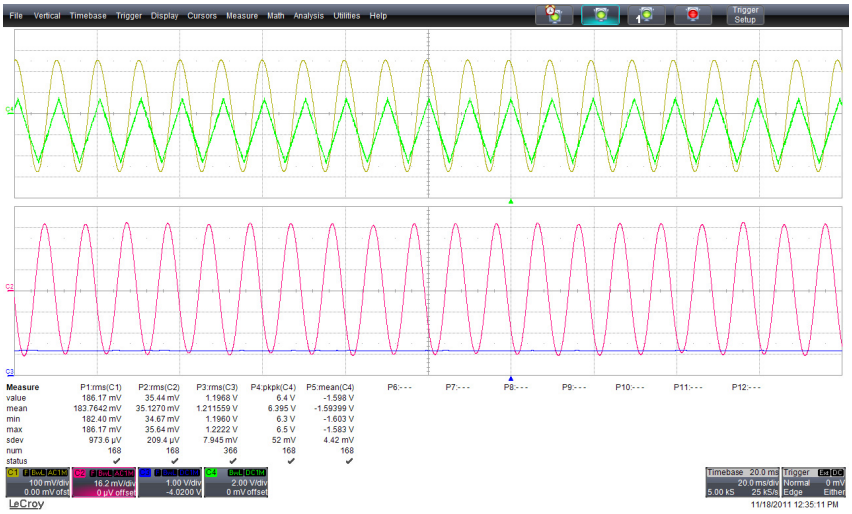

Figure 5-11: A screen shot of the digital oscilloscope.

Channel one (C1) shows the signal of the power reference, channel two (C2) is the detected probe laser signal, channel three (C3) is from the wavelength output port of the tunable laser, and channel 4 (C4) depicts the optical modulator driving signal from the signal generator. The tunable laser was set to scan from 1515nm to 1570nm with 0.2nm step. At each step, the oscilloscope captured 0.5 second data, which corresponded to 50 cycles of the 100Hz modulation signal and calculated the root mean square (rms) values of the C1 and C2 signals. After an entire scan was finished, the curve of rms(C2) versus wavelength was normalized to the maximum of rms(C1) and plotted. Since the amplitude of detected probe laser power is inversely proportional to the absorption of the oil cell, given the amount of relative absorption variation is small, which is true for a short cell, the normalized rms(C2) is in linear scale.

5.7 C_2H_2 Detection Cross Sensitivity Test over CH_4

To test the system response to a larger dynamic range, experiments on transformer oil, Voltesso 35, with dissolved acetylene at concentrations of 1%, 10% and 20% were conducted. Figure 5-12, shows the normalized photothermal signals measured at different

concentrations of acetylene. Because of the relatively large error on the oil preparation, especially for 1% C_2H_2 oil, the linearity of the detection results was somewhat degraded.

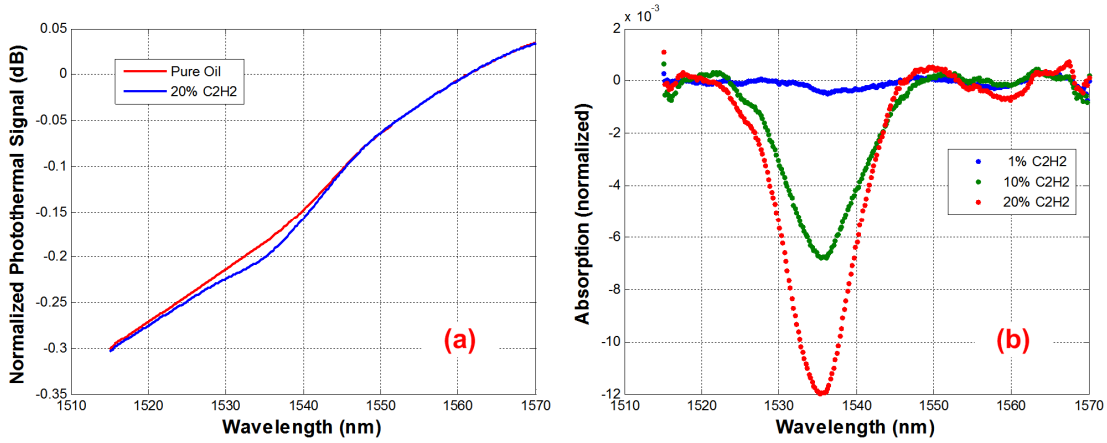

Figure 5-12: Photothermal signals of Voltesso 35 with C_2H_2 dissolved.

Experiment results on the cross sensitivity test with certain concentrations of methane are shown in Figure 5-13. Oil with 10% acetylene dissolved was chosen for the test. Although 1%, 5% and 10% methane were dissolved into oil (the relative concentration to acetylene were 10%, 50% and 100% respectively), no obvious error on the acetylene detection was observed, which confirmed that this method hardly has cross sensitivity with dissolved methane.

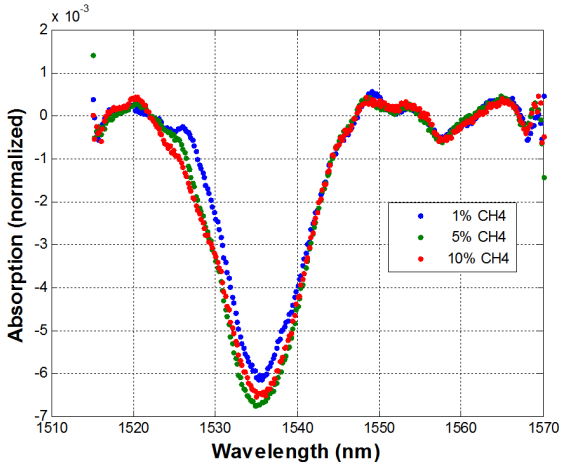

Figure 5-13: Methane cross sensitivity test results.

5.8 Conclusions and Directions for Improvement

Acetylene concentration detection by dissolved acetylene induced oil transmission loss is a newly developed method. Because this technique does not need the gas extraction procedure, it is thus possible to measure the concentration of acetylene by shooting a laser beam into the transformer oil through the sight glass mounted on the bushing and detecting the generated thermal or acoustic signal. Experiment results shown above indicate the feasibility of this method. The limited accuracy is mainly due to the poor stability and low power of the present available tunable laser. A high power swept laser may solve this problem in the future.

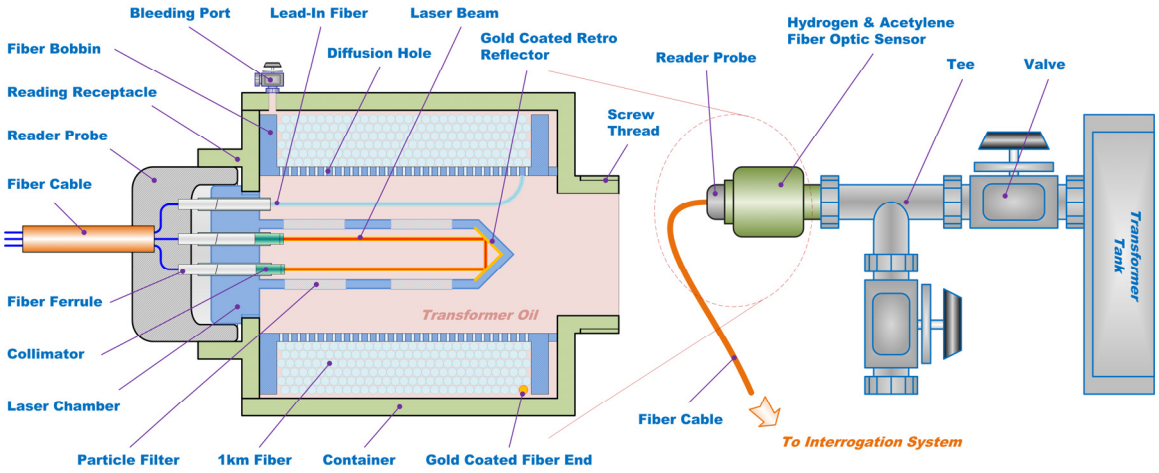

Figure 5-14: Schematic of the hydrogen and acetylene sensor prototype.

Based on the hydrogen and acetylene detection methods discussed in this dissertation, a sensor prototype for both gases detection has been designed and fabricated. As shown in Figure 5-14, the prototype consists of a spool of 1km optical fiber and an acetylene detection chamber at the center. Because of its compact size, low cost and standard connection interface, its applications can encompass all oil-insulated equipment, including instrument transformers, underground apparatus, cables and perhaps even bushings. Figure 5-15(a) gives an angled view of the fabricated prototype and Figure 5-15(b) was taken during its hydrogen detection test.

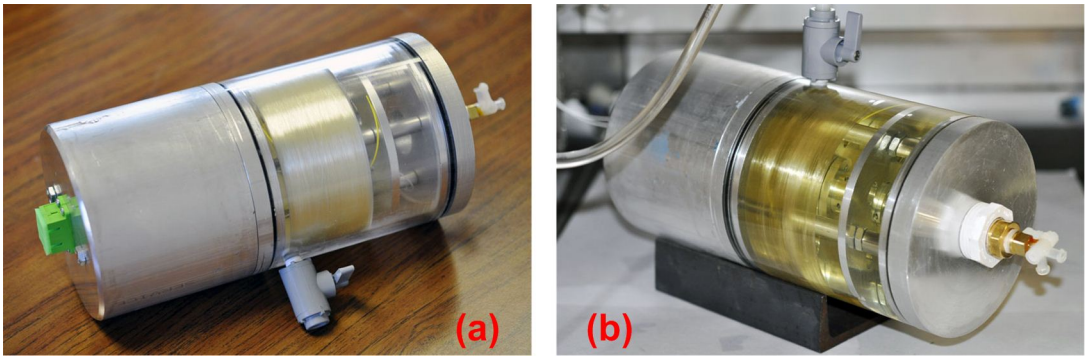

Figure 5-15: Pictures of the sensor prototype. (a) An angled view; (b) filled with oil.

CHAPTER 6

Summary

The reliability of diaphragm based EPRI fiber optics acoustic sensors has been proven by the previous field tests. By filling SF_6 into the inevitable FP cavity and using CO_2 laser thermal bonding technique, the newly fabricated sensor has been tested to be safe (without any discharge or partial discharge) in transformer oil between two electrodes with stress of 10kV/mm (AC rms value) applied, which is at least three times larger than that of a traditional EFPI fiber-optic sensor filled with air at ambient pressure and it is also 1.7 times of the maximum electric stress in operating power transformers.

Multiple-sensor PD detection is not only more reliable than single point detection but also PD location traceable. The presented two-wavelength quadrature detection mechanism and sensor cavity length control technique replaced expensive tunable filters or lasers with two low cost DFB lasers and CWDM add/drop filters, which enhanced the system stability and, at the same time, reduced system cost by at least 10 times.

Although the hydrogen induced fiber loss has been studied since 1970's and it was treated as a drawback for fiber communications, it was the first time that this effect had been used for hydrogen detection. Because of the intrinsic dielectric property of optical fibers, the sensor is able be installed inside operating power transformers for localized hydrogen concentration detection.

For the first time the spectrum of acetylene dissolved in transformer oil had been discovered, studied, and applied for acetylene concentration detection. No cross detection sensitivity to methane has been found with this method.

Despite of the relatively low resolution of the newly developed dissolved gas detection methods, which is mainly due to the limitation of light sources available at CPT; because

of their unique advantages, such as sample-less detection, minimum cross sensitivity to other gases, instant response, and low system cost, they will become very powerful competitors to the traditional DGA methods.

With the help of more accurate and prompt information from these on-line and real time acoustic and gaseous sensors, people will become more confident to make correct and wise decision on the health state of transformers to avoid any possible large scale damages and disasters.

REFERENCE

1. Bartley, W.H., *Analysis of Transformer Failures.* Preceedings of International Association of Engineering Insurers 36th Annual Conference – Stockholm, 2003.
2. Meunier, R. and G.H. Vaillancourt. *Propagation behaviour of acoustic partial discharge signals in oil-filled transformers*. in *Conduction and Breakdown in Dielectric Liquids, 1996, ICDL '96., 12th International Conference on*. 1996.
3. Teunissen, J., et al. *Fiber optical online monitoring for high-voltage transformers*. in *Fiber Optic Sensor Technology II*. 2001. Boston, MA, USA: SPIE.
4. Boggs, S.A., *Partial discharge: overview and signal generation.* Electrical Insulation Magazine, IEEE, 1990. **6**(4): p. 33-39.
5. Kreuger, F.H., *Partial discharge detection in high-voltage equipment*1989: Butterworth-Heinemann.
6. Lundgaard, L.E., *Partial discharge. XIV. Acoustic partial discharge detection-practical application.* Electrical Insulation Magazine, IEEE, 1992. **8**(5): p. 34-43.
7. Xiaodong, W., et al., *Acousto-optical PD detection for transformers.* Power Delivery, IEEE Transactions on, 2006. **21**(3): p. 1068-1073.
8. Schwarz, R., T. Judendorfer, and M. Muhr. *Review of Partial Discharge Monitoring techniques used in High Voltage Equipment*. in *Electrical Insulation and Dielectric Phenomena, 2008. CEIDP 2008. Annual Report Conference on*. 2008.
9. IEC-60270, *High-Voltage Test Techniques - Partial Discharge Measurements*, 2000.
10. Judd, M.D., Y. Li, and I.B.B. Hunter, *Partial discharge monitoring for power transformer using UHF sensors. Part 2: field experience.* Electrical Insulation Magazine, IEEE, 2005. **21**(3): p. 5-13.
11. Judd, M.D., Y. Li, and I.B.B. Hunter, *Partial discharge monitoring of power transformers using UHF sensors. Part I: sensors and signal interpretation.* Electrical Insulation Magazine, IEEE, 2005. **21**(2): p. 5-14.
12. Schwarz, R., M. Muhr, and S. Pack. *Partial discharge detection in oil with optical methods*. in *Dielectric Liquids, 2005. ICDL 2005. 2005 IEEE International Conference on*. 2005.
13. Muhr, M., R. Schwarz, and S. Jaufer. *Fibre optics in board arrangements with respect to partial discharge*. in *Electrical Insulation and Dielectric Phenomena, 2007. CEIDP 2007. Annual Report - Conference on*. 2007.
14. Schwarz, R. and M. Muhr. *Modern technologies in optical partial discharge detection*. in *Electrical Insulation and Dielectric Phenomena, 2007. CEIDP 2007. Annual Report - Conference on*. 2007.
15. Kawada, H., et al., *Partial Discharge Automatic Monitor for Oil-Filled Power Transformer.* Power Apparatus and Systems, IEEE Transactions on, 1984. **PAS-103**(2): p. 422-428.
16. Zhao, Z.Q., J.M.K. MacAlpine, and M.S. Demokan. *Directional sensitivity of a fibre-optic sensor to acoustic signals in transformer oil*. in *Advances in Power System Control, Operation and Management, 1997. APSCOM-97. Fourth International Conference on (Conf. Publ. No. 450)*. 1997.
17. Zhao, Z., M. MacAlpine, and M.S. Demokan, *The directionality of an optical fiber high-frequency acoustic sensor for partial discharge detection and location.* Lightwave Technology, Journal of, 2000. **18**(6): p. 795-806.
18. Deng, J., et al., *Optical fiber sensor-based detection of partial discharges in power transformers.* Optics & Laser Technology, 2001. **33**(5): p. 305-311.
19. Yu, B., et al., *Fiber Fabry-Perot Sensors for Detection of Partial Discharges in Power Transformers.* Appl. Opt., 2003. **42**(16): p. 3241-3250.
20. Wang, X., et al., *An ultra-sensitive optical MEMS sensor for partial discharge detection.* Journal of Micromechanics and Microengineering, 2005(3): p. 521.
21. Duval, M., *Dissolved gas analysis: It can save your transformer.* Electrical Insulation Magazine, IEEE, 1989. **5**(6): p. 22-27.
22. Duval, M. and A. dePabla, *Interpretation of gas-in-oil analysis using new IEC publication 60599 and IEC TC 10 databases.* Electrical Insulation Magazine, IEEE, 2001. **17**(2): p. 31-41.
23. Duval, M., *New techniques for dissolved gas-in-oil analysis.* Electrical Insulation Magazine, IEEE, 2003. **19**(2): p. 6-15.
24. Duval, M., *A review of faults detectable by gas-in-oil analysis in transformers.* Electrical Insulation

Magazine, IEEE, 2002. **18**(3): p. 8-17.
25. D. D. Chang, T.S.S., J. E. Thompson, *Analyis of electric stress distribution in cavities embedded within dielectric structures.* IEEE Tansactions on Electrica Insulation, 1986. **EI-21**(2): p. 213-219.
26. Gallagher, T.J., Pearmain, A. J. , *High voltage measurement, testing and design*1983: John Wiley and Sons Ltd. p63.
27. J. M. Meek, J.D.C., *Electrical Breakdown of Gases*1978: John Wiley & Sons, Ltd.
28. Raizer, Y.P., *Gas Discharge Physics*1997: Springer-Verlag Berlin Heidelberg New York.
29. T. Matsuo, K.H., R. Hata. *Coating effect on AC and impulse breakdown stress of SF_6.* in *Proceedings of 1998 International Symposium on Electrical Insulating Materials*. 1998. Toyohashi, Japan: Inst. Electr. Eng. Japan.
30. Juncheng, X., et al., *A novel temperature-insensitive optical fiber pressure sensor for harsh environments.* Photonics Technology Letters, IEEE, 2005. **17**(4): p. 870-872.
31. Dong, B., et al., *Sulfur hexafluoride-filled extrinsic Fabry-Perot interferometric fiber-optic sensors for partial discharge detection in transformers.* IEEE Photonics Technology Letters, 2008. **20**(18): p. 1566-1568.
32. Sheem, S.K., T.G. Giallorenzi, and K. Koo, *Optical techniques to solve the signal fading problem in fiber interferometers.* Appl. Opt., 1982. **21**(4): p. 689-693.
33. Yu-Lung, L., *In-fiber Bragg grating sensors using interferometric interrogations for passive quadrature signal processing.* Photonics Technology Letters, IEEE, 1998. **10**(7): p. 1003-1005.
34. Kersey, A.D., D.A. Jackson, and M. Corke, *Passive compensation scheme suitable for use in the single-mode fibre interferometer.* Electronics Letters, 1982. **18**(9): p. 392-393.
35. Murphy, K.A., et al., *Quadrature phase-shifted, extrinsic Fabry-Perot optical fiber sensors.* Opt. Lett., 1991. **16**(4): p. 273-275.
36. Santos, J.L. and D.A. Jackson, *Passive demodulation of miniature fiber-optic-based interferometric sensors using a time-multiplexing technique.* Opt. Lett., 1991. **16**(15): p. 1210-1212.
37. Koo, K.P., A.B. Tveten, and A. Dandridge, *Passive stabilization scheme for fiber interferometers using (3 x 3) fiber directional couplers.* Applied Physics Letters, 1982. **41**(7): p. 616-618.
38. Stowe, D. and H. Tsung-Yuan, *Demodulation of interferometric sensors using a fiber-optic passive quadrature demodulator.* Lightwave Technology, Journal of, 1983. **1**(3): p. 519-523.
39. Niemeier, T. and R. Ulrich, *Quadrature outputs from fiber interferometer with 4 × 4 coupler.* Opt. Lett., 1986. **11**(10): p. 677-679.
40. Valis, T., et al., *Passive-quadrature demodulated localized-Michelson fiber-optic strain sensor embedded in composite materials.* Lightwave Technology, Journal of, 1991. **9**(4): p. 535-544.
41. Giulianelli, L.C. and A.B. Buckman, *Fiber-optic circuit for direct phase conversion with two outputs in quadrature.* Lightwave Technology, Journal of, 1993. **11**(7): p. 1263-1265.
42. Kwon, I.-B., et al. *New digital processing algorithm for determining the direction and magnitude of the strain from quadrature phase-shifted fiber optic signals*. 1998. San Diego, CA, USA: SPIE.
43. Wright, O.B., *Stabilized dual-wavelength fiber-optic interferometer for vibration measurement.* Opt. Lett., 1991. **16**(1): p. 56-58.
44. Dahlem, M., et al., *Passive interrogation of low-finesse Fabry-Perot cavities using fiber Bragg gratings.* Photonics Technology Letters, IEEE, 2001. **13**(9): p. 990-992.
45. Fürstenau, N., et al., *Dynamic Pressure Sensing with a Fiber-Optic Polarimetric Pressure Transducer with Two-Wavelength Passive Quadrature Readout.* Appl. Opt., 1998. **37**(4): p. 663-671.
46. Furstenau, N. and M. Schmidt, *Interferometer vibration sensor with two-wavelength passive quadrature readout.* Instrumentation and Measurement, IEEE Transactions on, 1998. **47**(1): p. 143-147.
47. Schmidt, M., et al., *Fiber-optic extrinsic Fabry-Perot interferometer strain sensor with <50 pm displacement resolution using three-wavelength digital phase demodulation.* Opt. Express, 2001. **8**(8): p. 475-480.
48. Jiang, Y., C. Tang, and G. Guo, *Note: Phase compensation in the fiber optical quadrature passive demodulation scheme.* Review of Scientific Instruments, 2010. **81**(4): p. 046108-3.
49. Pinto, A.M.R., et al., *Interrogation of a Suspended-Core Fabry–Perot Temperature Sensor Through a Dual Wavelength Raman Fiber Laser.* Lightwave Technology, Journal of, 2010. **28**(21): p. 3149-3155.
50. Xu, J., et al. *Epoxy-free high-temperature fiber optic pressure sensors for gas turbine engine*

applications. 2004. Philadelphia, PA, USA: SPIE.
51. Steffes, M., *Noise Analysis for High-Speed Op-Amps*, in *Application Report* Jan, 2005, Texas Instruments.
52. *Noise Analysis of FET Transimpedance Amplifiers*, in *Application Bulletin* 2000, Burr-Brown.
53. Azad, A.M., et al., *Solid-State Gas Sensors: A Review.* Journal of The Electrochemical Society, 1992. **139**(12): p. 3690-3704.
54. Zanini, M., et al., *Fabrication and properties of a Si-based high-sensitivity microcalorimetric gas sensor.* Sensors and Actuators A: Physical, 1995. **48**(3): p. 187-192.
55. Shin, W., et al., *Thermoelectric Thick-Film Hydrogen Gas Sensor Operating at Room Temperature.* Japanese Journal of Applied Physics, 2001. **40**(Part 2, No. 11B): p. L1232.
56. McAleer, J.F., et al., *Tin dioxide gas sensors: use of the seebeck effect.* Sensors and Actuators, 1985. **8**(3): p. 251-257.
57. Huang, H., et al., *Thermoelectric hydrogen sensor working at room temperature prepared by bismuth-telluride P-N couples and Pt/[gamma]-Al2O3.* Sensors and Actuators B: Chemical, 2008. **128**(2): p. 581-585.
58. Houlet, L.F., et al., *Fabrication and performance of free-standing hydrogen gas sensors.* Sensors and Actuators B: Chemical, 2008. **129**(1): p. 1-9.
59. Shin, W., et al., *Hydrogen-selective thermoelectric gas sensor.* Sensors and Actuators B: Chemical, 2003. **93**(1-3): p. 304-308.
60. Frederick A. Lewis, K.K., X.Q. Tong, *Platinum and Palladium-Hydrogen: Lattice Structure and Expansion Effects.* Solid State Phenomena, 2000. **73-75**: p. 366-422.
61. Maier, R.R.J., et al., *Palladium-based hydrogen sensing for monitoring of ageing materials.* Measurement Science and Technology, 2006(5): p. 1118.
62. Michael, B., et al., *Active Fiber Bragg Grating Hydrogen Sensors for All-Temperature Operation.* Photonics Technology Letters, IEEE, 2007. **19**(5): p. 255-257.
63. Lin, H., et al., *A porous silicon-palladium composite film for optical interferometric sensing of hydrogen.* Langmuir, 2004. **20**(12): p. 5104-5108.
64. Greene, J.A., et al. *Applications of the extrinsic Fabry-Perot interferometer*. 1995. USA: SPIE-Int. Soc. Opt. Eng.
65. Butler, M.A. and D.S. Ginley, *Hydrogen sensing with palladium-coated optical fibers.* Journal of Applied Physics, 1988. **64**(7): p. 3706-12.
66. Chadwick, B. and M. Gal, *Enhanced optical detection of hydrogen using the excitation of surface plasmons in palladium.* Applied Surface Science, 1993. **68**(1): p. 135-138.
67. Zhao, Z., et al., *All-optical hydrogen sensor based on a high alloy content palladium thin film.* Sensors and Actuators, B: Chemical, 2006. **113**(1): p. 532-538.
68. Villatoro, J. and D. Monzon-Hernandez, *Fast detection of hydrogen with nano fiber tapers coated with ultra thin palladium layers.* Optics Express, 2005. **13**(13): p. 5087-5092.
69. Guemes, J.A., et al. *Comparison of three types of fibre optic hydrogen sensors within the frame of CryoFOS project*. 2005. USA: SPIE - The International Society for Optical Engineering.
70. Maciak, E., Z. Opilski, and M.W. Urbanczyk. *Detection of hydrogen by means of a thin film interferometer Fabry-Perot applying a-WO3 layers*. 2003. USA: SPIE-Int. Soc. Opt. Eng.
71. Opilski, Z. and E. Maciak. *Determination of the optical parameters of thin palladium layers and their application in optical hydrogen sensors*. 2004. Krasnobrod, Poland: SPIE.
72. Trouillet, A., E. Marin, and C. Veillas, *Fibre gratings for hydrogen sensing.* Measurement Science and Technology, 2006(5): p. 1124.
73. Maier, R.R.J., et al., *Fibre optics in palladium-based hydrogen sensing.* Journal of Optics A: Pure and Applied Optics, 2007(6): p. S45.
74. Sakamoto, Y., et al., *Effect of carbon monoxide on hydrogen permeation in some palladium-based alloy membranes.* International Journal of Hydrogen Energy, 1996. **21**(11-12): p. 1017-1024.
75. Mochizuki, K., et al., *Behavior of hydrogen molecules adsorbed on silica in optical fibers.* Quantum Electronics, IEEE Journal of, 1984. **20**(7): p. 694-697.
76. Mochizuki, K., et al., *Influence of Hydrogen on Optical Fiber Loss in Submarine Cables.* Selected Areas in Communications, IEEE Journal on, 1984. **2**(6): p. 842-847.
77. Beales, K.J., D.M. Cooper, and J.D. Rush, *Increased attenuation in optical fibres caused by diffusion of molecular hydrogen at room temperature.* Electronics Letters, 1983. **19**(22): p. 917-919.
78. Fox, M. and S.J. Stannard-Powell, *Attenuation changes in optical fibres due to hydrogen.*

Electronics Letters, 1983. **19**(22): p. 916-917.
79. Shackelford, J.F., P.L. Studt, and R.M. Fulrath, *Solubility of Gases in Glass. II. He, Ne, and H[sub 2] in Fused Silica.* Journal of Applied Physics, 1972. **43**(4): p. 1619-1626.
80. Graebner, J.E., et al., *Clustering of molecular hydrogen in fused silica.* Applied Physics Letters, 1985. **46**(9): p. 839-841.
81. Carslaw, H.S. and J.C. Jaeger, *Conduction of Heat in Solids*. 2nd ed1959: Oxford at the Clarendon Press.
82. Crank, J., *The Mathematics of Diffusion*. 2nd ed1975: Clarendon Press - Oxford.
83. Namihira, Y., K. Mochizuki, and M. Kuwazuru, *Temperature dependence of the hydrogen-diffusion constant in optical fibers.* Opt. Lett., 1984. **9**(9): p. 426-428.
84. Abramowitz, M. and I.A. Stegun, *Handbook of mathematical functions with formulas, graphs, and mathematical tables* 1972: Washington : U. S. Govt. Print. Off.
85. Vander Auwera, J., *Absolute intensities measurements in the N4+N5 band of 12C2H2: analysis of Herman-Wallis effects and forbidden transitions.* Journal of Molecular Spectroscopy, 2000. **201**(1): p. 143-50.
86. El Hachtouki, R. and J. Vander Auwera, *Absolute line intensities in acetylene: the 1.5-m region.* Journal of Molecular Spectroscopy, 2002. **216**(2): p. 355-62.
87. Cheung, A., W. Johnstone, and D. Moodie. *Detection of acetylene gas using optical correlation spectroscopy*. 2005. USA: SPIE - The International Society for Optical Engineering.
88. van Brakel, A., et al. *Photonic bandgap fiber optical correlation spectroscopy gas sensor*. 2008. USA: SPIE - The International Society for Optical Engineering.
89. Mizuno, K., et al., *Enhanced detection of gas absorption using an erbium-doped fiber ring laser.* Japanese Journal of Applied Physics, Part 1 (Regular Papers, Short Notes & Review Papers), 2002. **41**(8): p. 5458-62.
90. Ni, N., et al., *Enhancing the measurement accuracy of a cavity-enhanced fiber chemical sensor by an adaptive filter.* Measurement Science and Technology, 2008. **19**(11).
91. Okazawa, R., et al., *Sensitivity enhancement for acetylene detection at 1.5 m by use of a high-finesse optical cavity.* Japanese Journal of Applied Physics, Part 1 (Regular Papers, Short Notes & Review Papers), 1999. **38**(8): p. 4946-9.
92. Miklos, A., P. Hess, and Z. Bozoki, *Application of acoustic resonators in photoacoustic trace gas analysis and metrology.* Review of Scientific Instruments, 2001. **72**(4): p. 1937-1955.
93. Laurila, T., et al., *Cantilever-based photoacoustic detection of carbon dioxide using a fiber-amplified diode laser.* Applied Physics B (Lasers and Optics), 2006. **B83**(2): p. 285-8.
94. Webber, M.E., M. Pushkarsky, and C.K.N. Patel, *Fiber-Amplifier-Enhanced Photoacoustic Spectroscopy with Near-Infrared Tunable Diode Lasers.* Appl. Opt., 2003. **42**(12): p. 2119-2126.
95. Besson, J.P., S. Schilt, and L. Thevenaz, *Sub-ppm multi-gas photoacoustic sensor.* Spectrochimica Acta, Part A (Molecular and Biomolecular Spectroscopy), 2006. **63**(5): p. 899-904.
96. Hartwig, C.M., *Raman scattering from hydrogen and deuterium dissolved in silica as a function of pressure.* Journal of Applied Physics, 1976. **47**(3): p. 956-959.
97. Gordon, J.P., et al., *Long-Transient Effects in Lasers with Inserted Liquid Samples.* Journal of Applied Physics, 1965. **36**(1): p. 3-8.
98. Gupta, M., *Thermal diffusivity measurements using a pulsed dual?beam thermal lens technique.* Appl. Phys. Lett., 1980. **37**(6): p. 505.
99. Long, M.E., R.L. Swofford, and A.C. Albrecht, *Thermal lens technique: A new method of absorption spectroscopy.* Science, 1976. **191**(Copyright 1976, IEE): p. 183-5.